UNIVERSITY OF TWENTE.

Faculty of Science & Technology

Thermoelectric properties of vertically aligned nanocomposite films

Janiek van Slooten

BSc. Thesis

Advanced Technology

May 2021

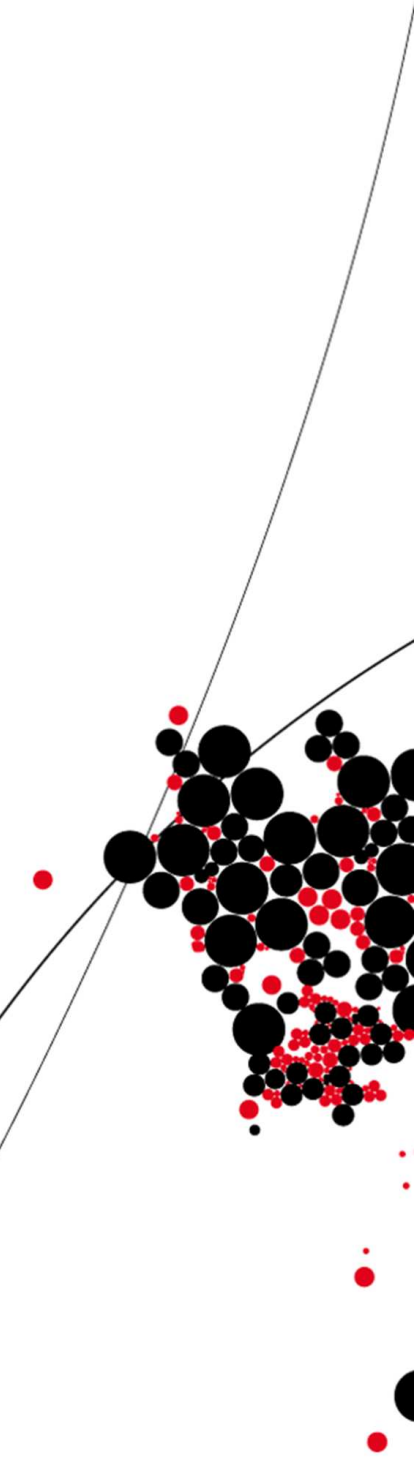

Supervisors:
Chair: prof. dr. ir. M. Huijben
Daily: M.W. van de Putte, MSc
External: A.J. Onnink, MSc

Inorganic Materials Science Group (IMS)
Faculty of Science & Technology

Abstract

Thermoelectric materials are a rapidly evolving research area as they are used in a wide range of applications. The optimizing of the thermoelectric properties is therefore of great interest. Using a new strategy with built in nanopillars, consisting of nanoparticles within a matrix of material, offer promising advantages as a key parameter, the thermal conductivity, could be lowered this way. The composite $(La_{0.7}Sr_{0.3}MnO_3)_{0.1} : (ZnO)_{0.9}$ is a candidate for promising thermoelectric properties. This composite was grown using pulsed laser deposition on 7 different substrates in order to investigate its growing behavior. The growth on a ZnO (0001) substrate showed the most promising results with a powerfactor ($S^2\sigma$) of $23.6\mu W/(cmK^2)$ which is in the range of the high-performance thermoelectric material Bi_2Te_3 at room temperature. [1] As seen on SEM images, it can be seen that the vertically aligned nanocomposite has been successfully grown on this sample. Clear LSMO pillars were observed within the ZnO matrix.

Nomenclature

Abbreviations

AFM	Atomic force microscopy
BHF	Buffered NH_4F-HF
DSO	$DyScO_3$
IMS	Inorganic Materials Science
IoT	Internet of Things
LSMO	$La_{0.7}Sr_{0.3}MnO_3$
NSO	$NdScO_3$
PF	Thermoelectric power factor ($S^2\sigma$)
PLD	Pulsed laser deposition
SEM	Scanning electron microscope
SPS	Smart Parking Systems
STO	$SrTiO_3$
TE	Thermoelectric element
TEG	Thermoelectric generator
UB	Ultrasonic bath
VAN	Vertically aligned nanocomposite
XRD	X-Ray diffraction
ZT	Order of merit ZT

Physical parameters

κ	Thermal conductivity	$[Wm^{-1}K^{-1}]$
κ_{el}	Electronic thermal conductivity	$[Wm^{-1}K^{-1}]$
κ_{lat}	Lattice thermal conductivity	$[Wm^{-1}K^{-1}]$
λ	Wavelength	$[nm]$
μ	Carrier mobility	$[cm^2/(Vs)]$
ρ	Electrical resistivity	$[\Omega m]$
σ	Electrical conductivity	$[S/m]$
B	Magnetic field	$[T]$
E	Electric field	$[V/m]$
F_L	Lorentz Force	$[N]$
h	Planck constant	$[6.626 * 10^{-34} Js]$
k_b	Boltzmann constant	$[1.38 * 10^{-23} JK^{-1}]$
m^*	Effective mass	$[kg]$
N	Integer	$[-]$
n	Carrier concentration	$[cm^{-3}]$
q	Elementary charge	$[\pm 1.602 * 10^{-19} C]$
R	Resistance	$[\Omega]$
R_s	Sheet resistance	$[\Omega]$
S	Seebeck coefficient	$[\mu V/K]$
T	Temperature	$[K]$
V	Electric potential	$[J/C]$

Contents

Chapter 1

Introduction

Current day technology keeps making life easier for us. Using the internet, everything can be connected with each other, not only computers but all devices that have internet protocols. This evolution is also called the Internet of Things (IoT) and has provided smart solutions like improving home security, introducing self-healing machines and assisting in the health and fitness of an individual. [2]

Another example of such a problem which needs a smart approach is the increasing parking problems in big cities. By using Smart Parking Systems (SPS), the presence of a car in a parking spot can be actively measured, processed and sent to a database. From this data, drivers are able to find parking spots with more ease and thus tackle this rising problem. The sensors detecting whether a car is parked need a power source in order to measure and send the needed data. In order to circumvent the use of batteries, which needs replacing every now and then, it would be more ideal to use a thermoelectric generator (TEG). This element can generate power as a result of a temperature difference and thus evades the use of lithium batteries. Besides replacing batteries in sensors, TEG's can also be used to convert waste heat into electrical energy in for example big industries. In order to let these devices work properly in different environments, research needs to be done to optimize the thermoelectric properties. [3] [4] [5]

1.1 Current research

Currently, a lot of research is being done in order to increase the performance of a thermoelectric element (TE). The performance of a TE, which is indicated by the ZT value, is hard to optimize as the combination of material with a high electrical conductivity and a low thermal conductivity is quite rare. The performance value ZT is defined as follows: $ZT = \sigma S^2 T/(\kappa_{el} + \kappa_{lat})$, where σ is the electrical conductiv-

ity, S is the Seebeck coefficient, T is the temperature, κ_{el} is the electronic thermal conductivity and κ_{lat} is the lattice thermal conductivity. [6] The relation between the temperature difference and an electrical potential, where the relation between these two are given by: $\Delta V = S\Delta T$, depends on the Seebeck coefficient. In order to achieve a high performance rate at a certain temperature it can easily be seen that a high σ and S is needed and a low κ is required.
A lot of research has been conducted in order to optimize thermoelectric materials, so much is known in this field of work and high ZT values have already been found. However, the relation between a high thermal- and electrical conductivity seems very coupled. Consequently, a new strategy was found using built-in nanostructures, to reduce thermal conductivity without influencing the electrical conductivity too much, has shown potential and record high ZT values exceeding a value of 2. [6] This gives reason to believe that nanostructures in the form of vertically aligned nanocompsites (VAN's) also has potential to lower the thermal conductivity. In figure 1.1 an example of a VAN material can be seen. VAN's can allow for effective phonon scattering in a significant portion of the phonon spectrum which results in a lower thermal conductivity.
An interesting combination of materials for such a VAN is
$(La_{0.7}Sr_{0.3}MnO_3)_{1-x}$: $((Zn_{0.98}Al_{0.02})O)_x$. [7] For Al doped ZnO of about 2% Al, the electrical conductivity becomes several orders of magnitude higher than the not doped variant and high S is observed. This results in record high powerfactors (PF, $S^2\sigma$). [8] The $La_{0.7}Sr_{0.3}MnO_3$ (LSMO) contribution is expected to reduce the thermal conductivity optimizing the ZT even further. To get a first impression of the material properties, ZnO will not be doped with Al yet.

The pillar size could influence the thermal conductivity as phonon scattering can be achieved at different wavelengths. In order to change the pillar size, certain parameters of growing the thin-film can be changed. Thin-films can be grown using pulsed laser deposition (PLD). With a lower frequency, the LSMO has more time to migrate and thus is expected to form bigger pillars. With a higher substrate temperature, the particles have a higher energy and it will be easier to migrate which again is expected to form bigger pillars. Thin-films with bigger pillars is expected to have a lower thermal conductivity, but still a high electrical conductivity, thus a high ZT value. The optimum of growing VAN thin-films needs to be found in order to maximize the performance. [6]

1.2 Thesis outline

The aim of this project is to grow LSMO pillars embedded in a matrix of ZnO using PLD. The growth of these VAN's will be researched using different substrates where

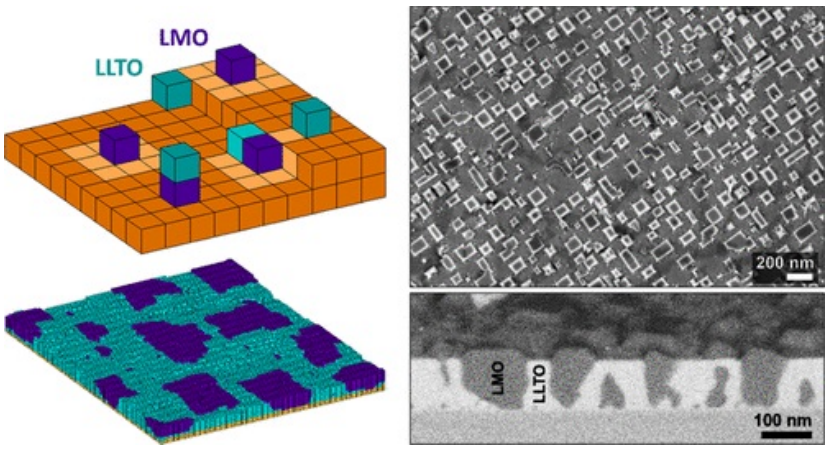

Figure 1.1: Top left image illustrates how a pillar (LMO) could orient itself over a matrix (LLTO) forming a VAN. Bottom left shows a simulation how the phases would align under certain conditions. Top right shows a top view and bottom right a cross-section scanning electron microscope (SEM) image of LMO pillars in a LLTO matrix [9]

growth parameters are kept constant. [9]

X-Ray diffraction (XRD) will be used to determine the crystal structure of the material and atomic force microscopy (AFM) will be used to obtain an image of the surface morphology. Scanning electron microscopy (SEM) will be used to obtain a image of a cross section of the grown sample, giving more insight of how the material has grown on the substrate. The Seebeck coefficient and electrical conductivity will be measured in order to determine the thermoelectric properties.

Chapter 2

Theory

In this chapter all relevant theoretical concepts will be explained. Starting with the design of a thermoelectric device and important properties needed to optimize this device. With these known parameters, the VAN strategy will be explained along sided proposed material combination and substrates used to grow on.

2.1 Thermoelectric effect

The electrical and thermal conductivity are closely linked and affect each other. This linkage is described in thermoelectricity. The first thermoelectric effect observed was the Seebeck effect in 1821. This effect can be visualized by figure 2.1. A ma-

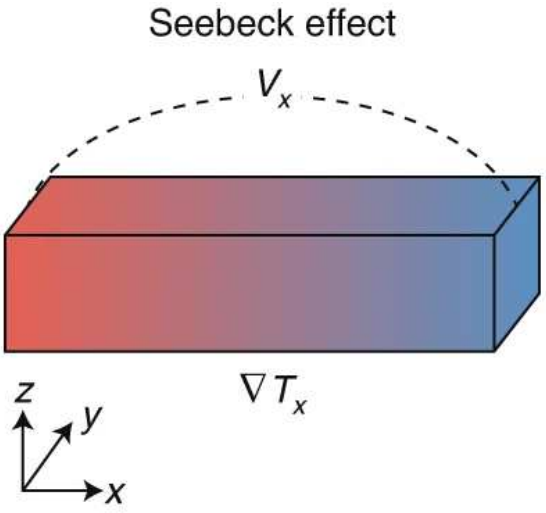

Figure 2.1: Schematic of the Seebeck effect in a single phase sample with a temperature gradient where red represents the hot side and blue the cold. [10]

terial, or multiple, in a certain configuration is heated on one side and cooled on the

other, applying a temperature gradient. Due to this temperature gradient, a potential difference ΔV can be measured. The relation between the potential difference and the temperature gradient is called the thermoelectric power, or Seebeck coefficient and is given by equation 2.1. This is not the only thermoelectric effect that occurs, but for now we will only discuss this particular effect as it suffics for our purposes.

$$\Delta V = S\Delta T \tag{2.1}$$

This thermoelectric effect is based on the charge carrier distribution in the material which are carrying heat and charge simultaneously. At the hot side of the material the charge carriers have a higher kinetic energy which results in a net velocity of the carriers to the cold side and will accumulate, building up a charge. This charge makes the carriers move back to the hot side. However, a net difference remains. When an equilibrium state is reached, the potential difference ΔV can be measured as seen in equation 2.1. Depending on whether the material in question is a p- or n-type semiconductor determines the type of charge carrier, either electrons or holes, and thus the sign of the potential.

2.2 Thermoelectric material properties

A combination of many small pieces of n- and p-type thermoelectric elements ordered as seen in figure 2.2a are wired electrically in series and thermally in parallel. The p-type material experiences a higher positive carrier concentration at the cold side, whereas the n-type experiences a negative build up of charge carriers. The electrons flow in the opposite direction of the current as seen in figure 2.2b and arrive at the p-type material. Since there is an electrostatic potential on the material, the electrons will diffuse towards the hot side where they can freely travel towards the n-type material. As the top of the n-type is positive, the electrons will want to enter the n-type material. There the thermoelectric effect takes place and thus the electrons again travel towards the cold side. Thus, when applying a temperature difference on such an element, a power will be generated. The maximum performance for this power generation is denoted by its figure of merit ZT (equation 2.2). [11] [12] [13]

$$ZT = \frac{\sigma S^2 T}{(\kappa_{el} + \kappa_{lat})} \tag{2.2}$$

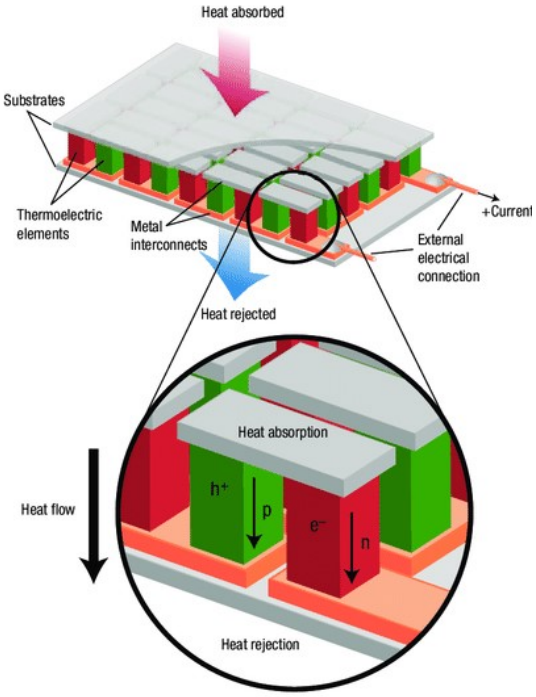

(a) Thermoelectric module. [13]

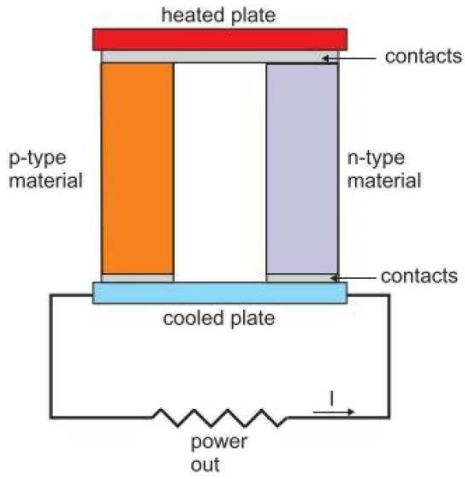

(b) Schematic overview of a single thermoelectric element. Adapted from Tilley. [12]

Figure 2.2: Two schematics of how thermoelectric materials are used in a TEG.

2.2.1 Maximizing ZT

To maximize the order of merit ZT, the optimization of various conflicting properties is needed. A large Seebeck coefficient is needed, alongside a high electrical conductivity and a low thermal conductivity. Low carrier concentration insulators and semiconductors have a high Seebeck coefficient but also a low electrical conductivity. The relationship between carrier concentration and Seebeck coefficient for metals and degenerate semiconductors can be approximated by equation 2.3. [13]

$$S = \frac{8\pi^2 k_B^2}{3qh^2} m^* T \left(\frac{\pi}{3n}\right)^{2/3} \tag{2.3}$$

Where k_b is the Boltzmann constant, q is the elementary charge, h is the Planck constant, m^* is the effective mass of the carrier and n is the carrier concentration. The electrical conductivity and resistivity are related to the carrier concentration as seen in equation 2.4 where μ is the carrier mobility.

$$1/\rho = \sigma = ne\mu \tag{2.4}$$

In figure 2.3 the relation between the different parameters in ZT is shown. A compromise of a high electrical conductivity and high Seebeck coefficient needs to be found. Typically, the peak of the ZT value lies at a carrier concentration between 10^{19} and 10^{21} carriers per cm^3 which falls in the heavily doped semiconductor regime.

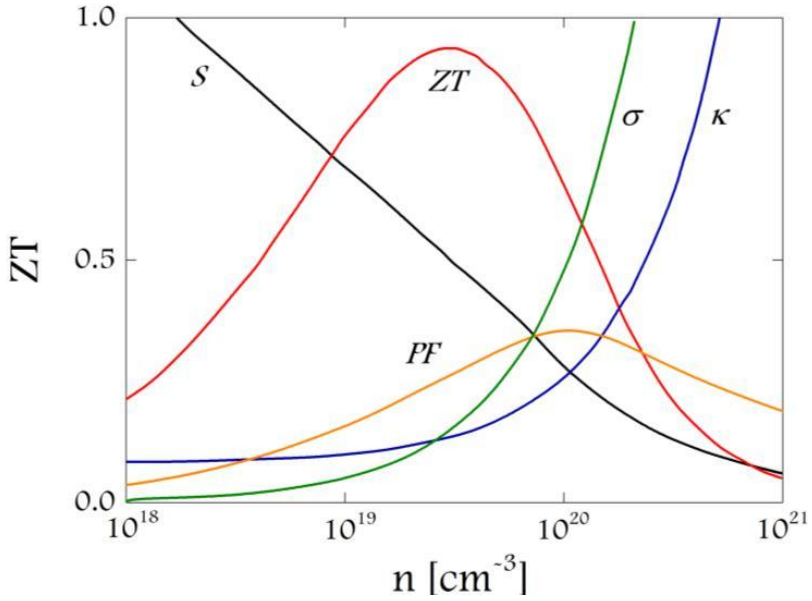

Figure 2.3: Optimizing ZT is a compromise between the Seebeck coefficient, electrical- and thermal conductivity as shown in this graphic. The thermoelectric power factor (PF) is defined as $S^2\sigma$ [14]

Apart from optimizing the electrical conductivity and the Seebeck coefficient, the necessity of a low thermal conductivity is also of high importance in order to achieve a high ZT. The thermal conductivity is a combination of the electronic thermal conductivity, which is the heat transported by electrons or holes, and the lattice thermal conductivity which are phonons travelling through the lattice. The electrical thermal conductivity is directly related to the electrical conductivity and thus is not wise to try to lower. The optimization therefore lies in the lattice thermal conductivity. The heat flow of phonons is carried by a spectrum of varying wavelengths and mean free paths as seen in figure 2.4a. In order to reduce the lattice thermal conductivity, phonon scattering at a variety of length scales is needed. Thus creating complexity in a material at multiple length scales whilst maintaining high electronic conductivity is a working strategy in order to achieve high ZT values as seen in figure 2.4b.
This can be done by introducing VAN's. It is expected that creating pillars in a nanostructure will contribute with the phonon scattering and thus lower the thermal conductivity. This strategy was for example used by R. Anufriev and used Aluminium nanopillars to lower the thermal conductivity by 20%. [15]

2.3 Substrates

The target material is deposited using PLD, which is a growing technique using a high density laser to deposit material from a target on various substrates (see

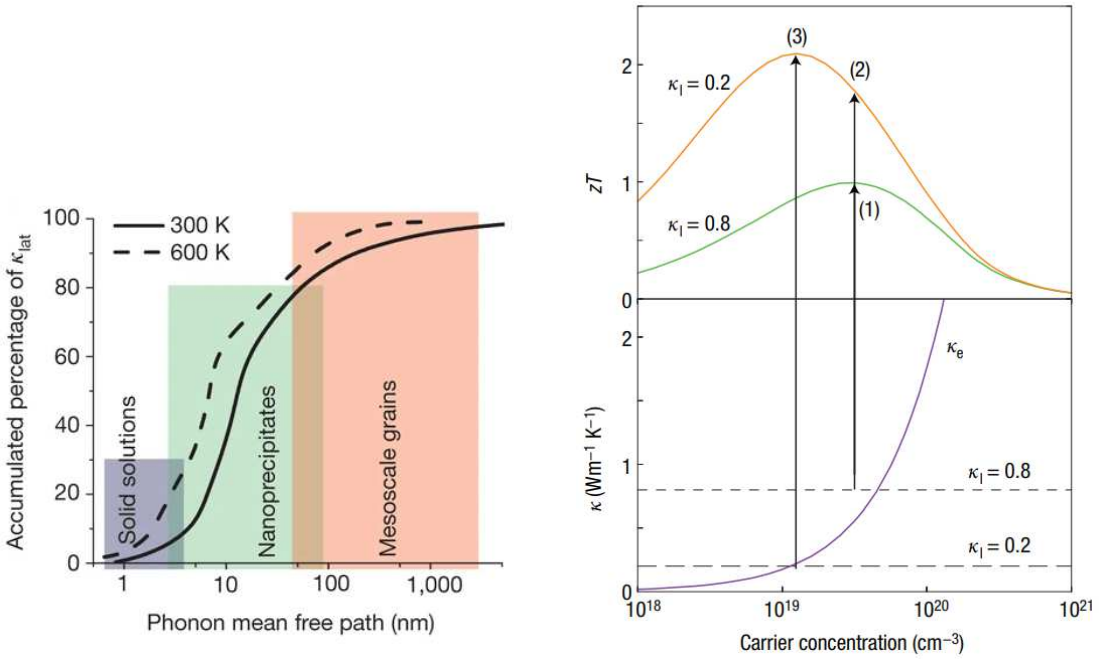

(a) Contributions of phonons with different free mean paths to the cumulative κ_{lat} value for PbTe. [6]

(b) A graphical representation of how lowering κ_{lat} increases the ZT. [13]

Figure 2.4: Two graphs showing the influence of the lattice thermal conductivity

section3.3). The target in question contains LSMO and ZnO with a 1 to 9 ratio. The expected crystal structure of LSMO is a perovskite cubic structure as seen in figure 2.5 and has a lattice parameter of 3.88Å. The perovskite oxide has the typical chemical formula ABO_3 where A and B are cations with a total charge of +6 and the oxygen elements have a total charge of -6. [16] ZnO has a hexagonal crystal structure where $a = b = 3.2650\text{Å}$ and $c = 5.2190\text{Å}$ as seen in figure 2.6. In this subsection the six different substrates on which material will be grown are discussed and a prediction on growth orientations will be given with the corresponding lattice mismatches. The grown material will always experience the lattice mismatch, as the material deposited can still orient itself.

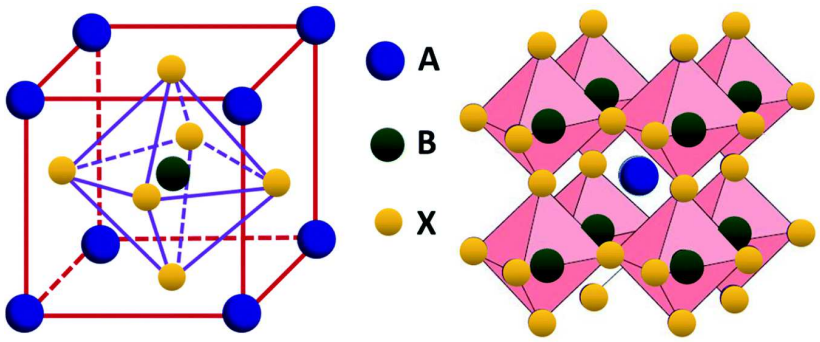

Figure 2.5: Typical perovskite cubic crystal structure. [17]

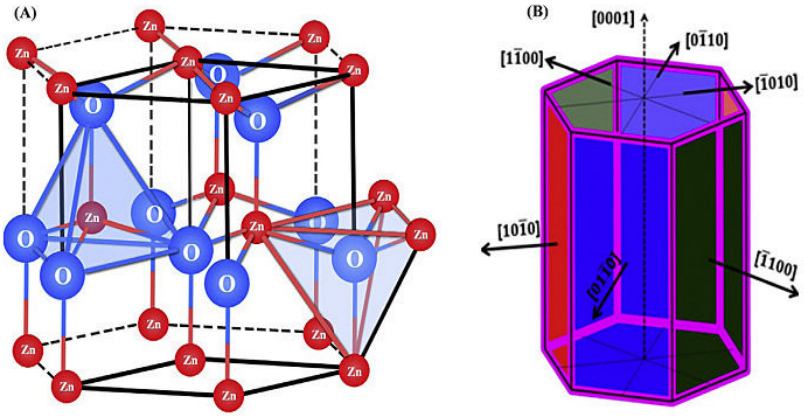

Figure 2.6: Hexagonal wurtzite structure ZnO. [18]

2.3.1 $SrTiO_3$ (001)

$SrTiO_3$ (STO) has a perovskite cubic crystal structure with a lattice parameter of 3.9050Å as seen in figure 2.7. Which closely matches the lattice of cubic LSMO of 3.88 Å. Thus the (001) plane of both perovskites have similar parameters resulting in a tensile lattice mismatch of 0.64%.
The lattice parameter of the STO crystal in the [110] direction is 5.52Å. The [1$\bar{1}$00] direction of hexagonal ZnO has a lattice parameter of 5.655 Å as matching parameter together with the [0001] direction which has a lattice parameter of 5.2190Å. These two directions correspond to the (11$\bar{2}$0) in plane ZnO, therefore it is expected that ZnO will grow in a 45° angle on the STO substrate as seen in figures 2.8a and2.8b. This orientation will grow with a compressing lattice mismatch of 2.40% in the [1$\bar{1}$00] direction and a tensile lattice mismatch of 5.50% in the [0001] direction. However, a (0001) ZnO phase is also possible where the [11$\bar{2}$0] direction with a lattice parameter of 5.655Å will fit the STO (001) diagonal with a lattice parameter of 5.52Å. This orientation has a higher mismatch and thus is expected to grow in lower orders with respect to the (11$\bar{2}$0) direction. [19]

2.3.2 $SrTiO_3$ (110)

For the STO (110), the dimensions change a bit. The plane gets a 5.52Å to 3.905Å ratio. As LSMO is a similar perovskite, it will change its orientation accordingly and thus there is expected it will also grow in the (110) orientation. The parameters for LSMO are 5.487Å to 3.88 Å resulting again in a 0.64% tensile lattice mismatch for the LSMO.
Presumably ZnO will grow in the (0001) in plane orientation. Where the a parameter

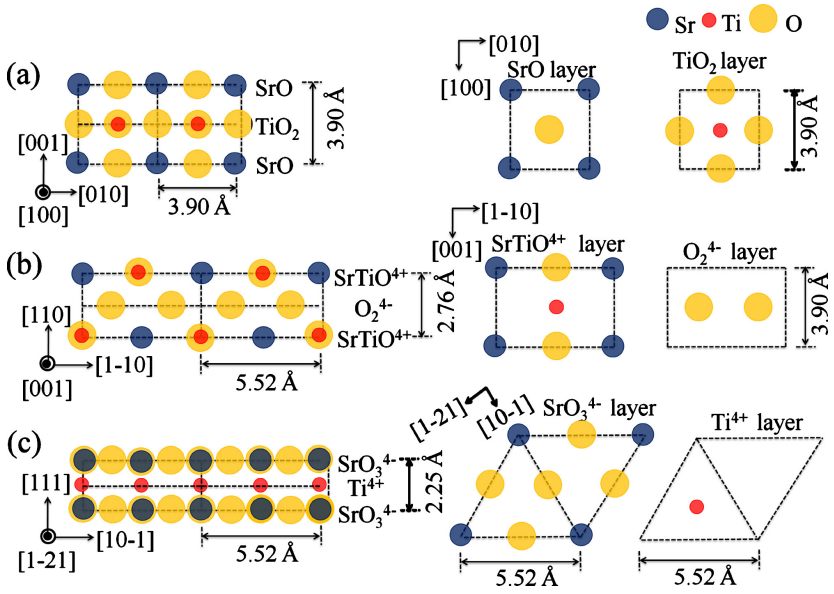

Figure 2.7: STO orientations schematic display. Left panel shows a cross-section and the right panel a top view for (001), (110) and (111) STO orientated substrates. [20]

of 3.265Å fits the a parameter of STO and the [1$\bar{1}$00] direction of ZnO with a width of 5.655Å fits the diagonal of 5.52Å as seen in figure 2.8c. Resulting in a tensile lattice mismatch of 16.39% in the a direction and a compressing lattice mismatch of 2.40% in the [1$\bar{1}$00] direction. [19]

2.3.3 $SrTiO_3$ (111)

STO (111) has a triangle like structure as seen in 2.7c. LSMO again has the opportunity to grow in the same (111) orientation with again a 0.64% tensile lattice mismatch.
The triangle like structure can be encapsulated by the hexagonal (0001) in plane growing orientation of ZnO as seen in figure 2.8d.The [1$\bar{1}$00] lattice parameter of 5.655Å fits with the triangle sides with lattice parameter 5.52Å resulting in a compressing lattice mismatch of 2.40%.

2.3.4 MgO (001)

MgO has a cubic crystal structure with a lattice parameter of 4.217Å. This case is similar as the STO (001) case and thus LSMO is expected to grow in the same (001) orientation. LSMO experiences a 7.99% compressing lattice mismatch.
ZnO again presumably grows in the (11$\bar{2}$0) in plain orientation, similar as the STO (001) case as also seen in figure 2.8b, resulting in a tensile lattice mismatch of

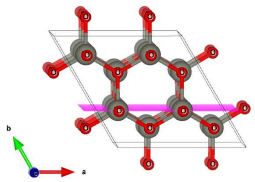

(a) $(11\bar{2}0)$ plane of ZnO.

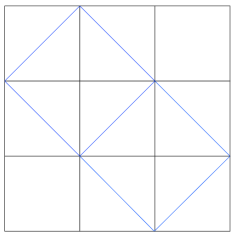

(b) Schematic of how ZnO is predicted to grow on STO (001) and MgO (001), in the $(11\bar{2}0)$ direction.

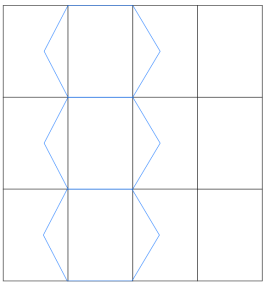

(c) Schematic of how ZnO is predicted to grow on STO (110), in the (0001) direction.

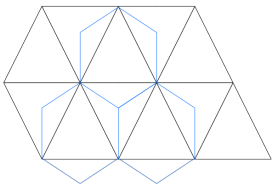

(d) Schematic of how ZnO is predicted to grow on STO (111), in the (0001) direction.

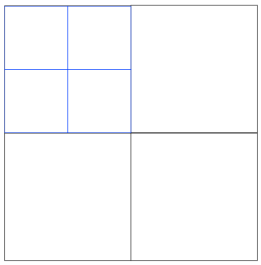

(e) Schematic of how LSMO is predicted to grow on DSO and NSO, in the (001) direction.

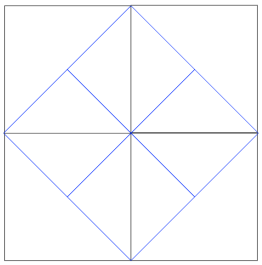

(f) Schematic of how ZnO is predicted to grow on DSO and NSO, in the $(11\bar{2}0)$ direction.

Figure 2.8: Different predicted growing orientations. The black lines represent the substrate in question whereas blue represents the material grown

5.18% in the $[1\bar{1}00]$ direction and a tensile lattice mismatch of 12.49% in the [0001] direction.

2.3.5 $DyScO_3$ (110)

$DyScO_3$ (DSO) has an orthorhombic crystal structure meaning that the three axes are perpendicular to each other but with each different lengths. Where in this case $a = 5.720\text{Å},\ b = 5.4490\text{Å}\ \&\ c = 7.9130\text{Å}$. In the (110) plane this results in a rectangle structure with parameters 7.913Å to 7.900Å. LSMO (001) can grow side by side on this structure, as seen in figure 2.8e as LSMO (001) has lattice parameter 3.88Å and twice this matches the c lattice parameter of DSO with a tensile lattice mismatch of 1.94%. The same holds for the [110] of DSO but with a tensile lattice mismatch of 1.77%

A ZnO fits with a 45° angle on DSO in the $(11\bar{2}0)$ plain as seen in figure 2.8f. Where the diagonal of ZnO with lattice parameter 7.695Å fits the [110] direction of DSO with a tensile lattice mismatch of 2.59% and the lattice parameter c with a tensile lattice mismatch of 2.75%.

2.3.6 $NdScO_3$ (110)

$NdyScO_3$ (NSO) is a very similar material as DSO. Therefor the same grow is expected. The lattice parameters of NSO are $a = 5.770\text{Å},\ b = 5.5810\text{Å}\ \&\ c = 8.0070\text{Å}$. LSMO will grow in the same fashion as with DSO but with a tensile lattice mismatch of 3.08% and 3.33% respectively.
The ZnO will experience a tensile lattice mismatch of 4.14% on the [110] direction of NSO and 3.90% on the c lattice parameter of NSO.

2.3.7 ZnO (0001)

ZnO will grow well on ZnO in the same orientation without experiencing a lattice mismatch. LSMO will favor the (110) plane where a parameter of both materials will match with a compressing lattice mismatch of 18.84% and the diagonal of the LSMO (001) will match the $[1\bar{1}00]$ direction with a tensile lattice mismatch of 2.97%.

Chapter 3

Experimental

This chapter includes the various techniques used for the growing and preparing of the samples as well as the techniques used for determination of structural and thermoelectric properties of made samples.

3.1 Atomic force microscopy

The AFM belongs to the scanning probe microscopes and is able to image the topography of a conducting or insulating sample with atomic resolution. The sample is scanned by a sharp tip, which is mounted to a cantilever spring made of silicon. The deflection or oscillation amplitude of the cantilever, as a result of the force between the sample and the tip, is measured with a very accurate laser and sensitive detector. Detected changes in deflection or oscillation amplitude can be corrected to a setpoint value with a feedback-controlled piezo element. With this correction, the sample tip distance can be held constant reducing possible damage on either the sample or the tip. This correction value is correlated with the height of the sample. Combined with the XY coordinate, a topographic image can be created with resolutions to 0.06nm [21]. A schematic setup can be found in figure 3.1a. A typical image scanned by a AFM system can be found in figure 3.1b. [22] [23]

3.2 Substrate treatment

In order to allow controlled growth on a substrate, it is of great importance that the substrate is atomically flat. Therefore, it is important to treat them accordingly before the deposition. Each of the substrates have a different chemical or annealing treatment. For verification means, all substrates are checked after treatment using AFM imaging techniques as discussed in section 3.1 and are processed using

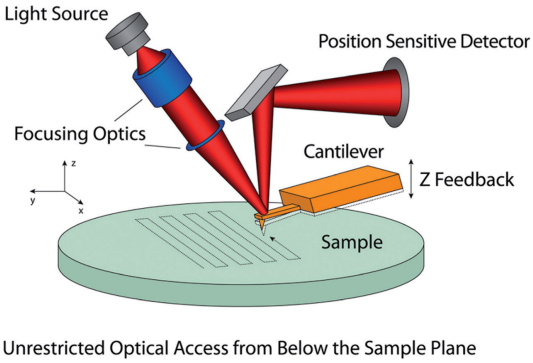

(a) Schematic drawing of a atomic force microscope. Light is reflected off of the back of the cantilever and on highly accurate detector. Scanning raster wise the topography of the sample is measured. [21]

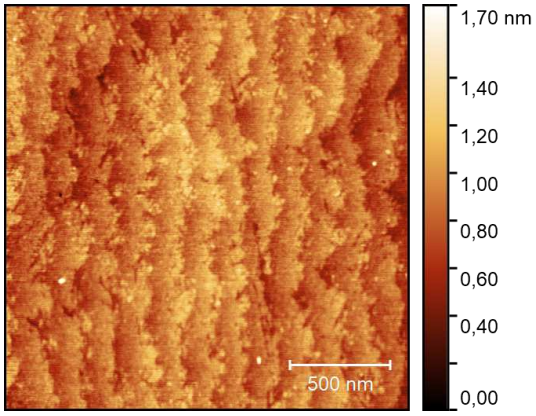

(b) AFM image of STO (001) before annealing 2x2 μm

Gwyddion software. In table 3.1 it can be seen that all substrates have a sufficiently low roughness and thus have been treated successfully.

Table 3.1: The roughness of the substrates extracted from AFM images using Gwyddion software

Treated substrates	RMS roughness (nm)
DSO (110)	0.2
MgO (001)	0.6
NSO (110)	0.2
STO (001)	0.2
STO (110)	0.3
STO (111)	1.0
ZnO (0001)	0.2

3.2.1 STO treatment

The three different orientations of STO have similar annealing treatments, however the chemical treatment is only used on the (001) substrate and is skipped for the (110) and (111) substrates of STO.

First of all, all three substrates are immersed in a ultrasonic bath (UB) using acetone and ethanol separately for 10 minutes. In between the samples are cleaned using a lens tissue and dried with a nitrogen gun and checked under the microscope. Uniquely for the STO (001) substrate, it is etched using buffered NH_4F-HF (BHF) for 30 seconds in the UB. This etching removes the SrO layer of the STO as seen in figure 2.7, leaving the TiO_2 layer exposed. [19] Afterwards it is again cleaned, dried and checked under the microscope. After this procedure all substrates are annealed at 950℃ for 1.5 hours under a continuous oxygen flow (150mL/hr). As seen in the

images in figure 3.2, the STO substrates after treatment show clear terrace steps and atomically flat surfaces. In figure 3.3a the image has been edited in such a way that the terraces are aligned to be horizontal. Taking the height profile, as seen in figure 3.3b, it can clearly be observed that the terrace step size corresponds to one unit cell of STO being 3.905Å.

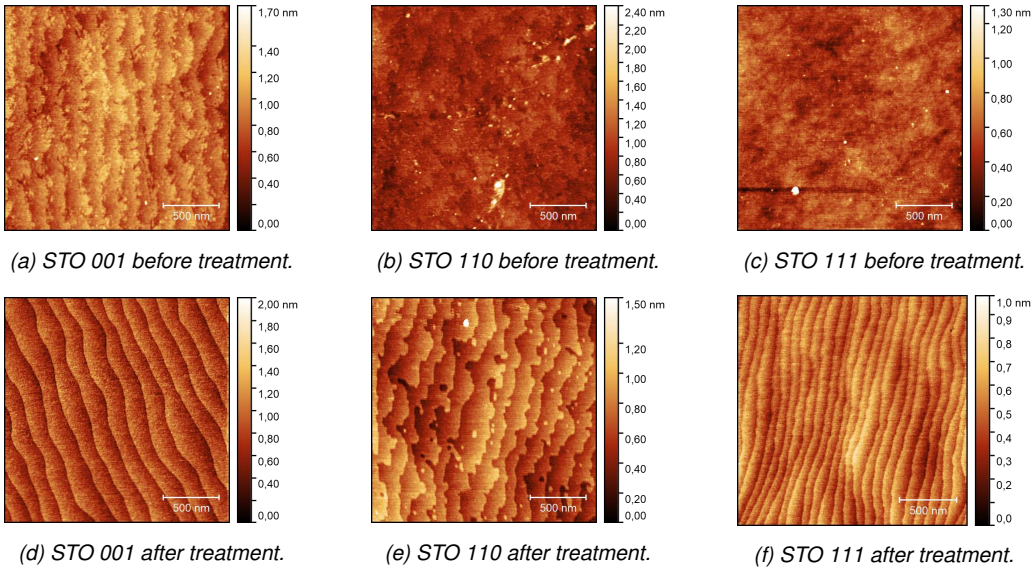

(a) STO 001 before treatment. *(b) STO 110 before treatment.* *(c) STO 111 before treatment.*

(d) STO 001 after treatment. *(e) STO 110 after treatment.* *(f) STO 111 after treatment.*

Figure 3.2: (a, b, c) AFM images of STO substrates before treatment. (d, e, f) AFM images of STO substrates after treatment.

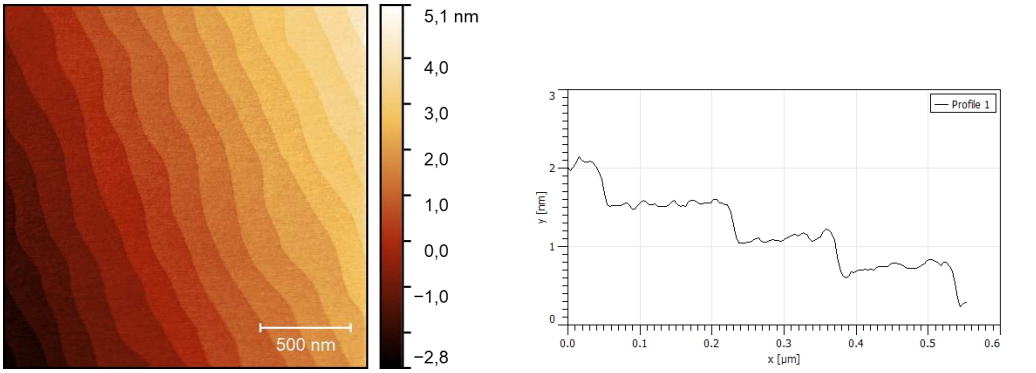

(a) AFM image edited where the terraces are flat. This way the terrace steps can be seen more clearly. *(b) Graph of height profile taken perpendicular on the terrace steps as seen in figure 3.3a*

Figure 3.3: Terraces of STO (001) substrate.

3.2.2 DSO and NSO treatment

DSO and NSO (110) have been treated in the same way to achieve a flat surface. First the substrates are immersed in an UB using acetone and ethanol separately for 10 minutes. Afterwards the substrates are cleaned, dried and checked under the

microscope. If the surfaces are free from particles, it is ready for the annealing. The substrates are annealed for 4 hours at 1000℃ in flowing oxygen (150mL/hr). After the samples are cooled down to room temperature, they are chemically treated. First, the substrates are immersed in deionized water in an UB for 30 minutes. After that, they are treated with BHF for 30 seconds in the UB. The substrates are cleaned and dried for the last step. The substrates first are etched with 12 M NaOH (aq) for 30 minutes in the UB and then again 30 minutes with 1 M NaOH (aq). For the last time, the substrates are cleaned and dried. Using this treatment, a flat substrate with a top layer of ScO_2 is the result. [24]

3.2.3 MgO and ZnO treatment

The MgO and ZnO substrates have been treated almost the same. Both first were immersed in acetone for 10 minutes in the UB, this step is repeated with ethanol. Afterwards both substrates were cleaned with a lens tissue and dried with a nitrogen gun. ZnO was annealed for 1 hour at 1000℃ with a constant oxygen flow of 150mL/hr. MgO was annealed for 2 hours at 900℃ in the same oxygen conditions.

3.3 Pulsed laser deposition

PLD is a often used technique to grow a thin layer on a substrate. A schematic of this technique is found in figure 3.4. High-power laser pulses are shot in a given frequency on a target evaporating small amounts of matter resulting in a laser plume normal to the target. The particles from the target are shot towards the substrate, creating a thin layer of this material. The substrate is often heated, in order to allow particle migration. [25]
For the deposition on the 7 different substrates, the same grow conditions have been used. The chamber experienced a $2.6 * 10^{-1} mbar$ oxygen background pressure. In total 10800 laser pulses at a rate of 5 Hz were shot on the LSMO ZNO 1 to 9 ratio target, which is estimated to grow a material layer of 240nm. The substrate was heated to 850℃.

3.4 Contact sputtering

In order to perform Seebeck and electrical conductivity measurements, Au/Ti contacts are sputtered on the samples. These contacts lower the resistance between the probes and the samples and allow for better measurements. The contacts are only needed in the four corners of the sample to perform all measurements, thus

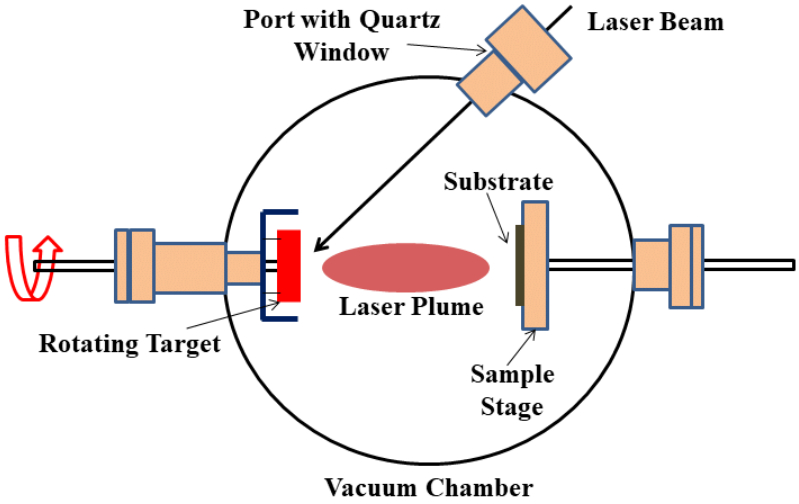

Figure 3.4: Schematic of PLD technique. [26]

a mask is placed over the sample in order to cover the rest of the sample. To improve the attachment of the golden contact, first a Ti layer of approximately 6nm is sputtered on the sample. Afterwards, the Au layer is sputtered on the sample with a thickness of about 100nm.
In order to grow the layer, the samples are put in a sputter setup. High energy ions, often Argon, are shot at a target. Because of this collision, atoms from the target are shot off and move towards the substrate. Using calibration methods, the growth rate can be controlled. In figure 3.5 a schematic overview can be seen. [27] [28]

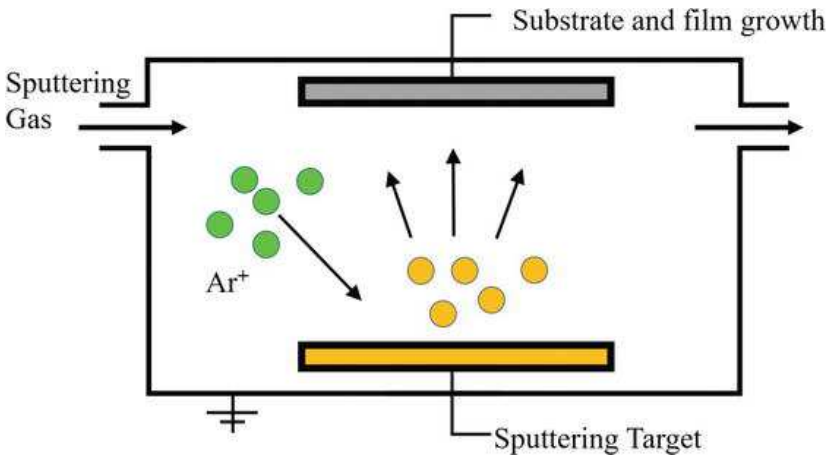

Figure 3.5: Schematic of a typical sputter deposition setup. [27]

3.5 X-ray diffraction

XRD is a measuring technique that uses x-rays to determine the crystal structure of a material. The technique relies on a phenomenon called diffraction. When waves are scattered by obstacles, the resulting waves interfere with each other. If this happens in an orderly matter, the resulting waves with a specific phase relationship is called diffraction. When two waves encounter each other with a path length difference equal to $N\lambda$, where N is a positive integer and λ is the wavelength, they will constructively interfere, meaning the amplitudes are additive. If the path length difference equals $(N + \frac{1}{2})\lambda$ the waves are exactly out of phase and they will destructively interfere, meaning that the resulting amplitude will be zero. Phase relations between these two extremes exist resulting in partially constructive or destructive interfering effects.
Using XRD, the x-ray beam will enter the sample, interact with the atoms in the material and scatter in all directions. However, the beams 1' and 2' as seen in figure 3.6 can constructively interfere if the path length difference QT is equal to a multiple of the wavelength. This results in Bragg's law as seen in equation 3.1 where θ is the angle between the plane and the incident beam and d is the interplanar spacing.

$$N\lambda = 2d\sin\theta \tag{3.1}$$

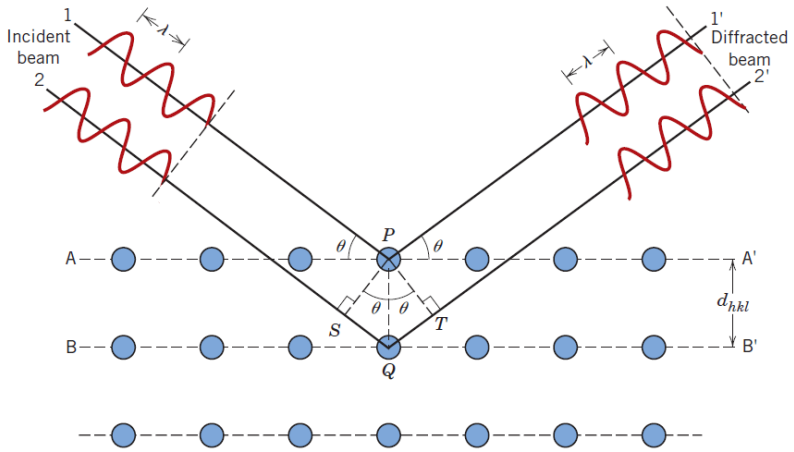

Figure 3.6: Diffraction of x-ray beams in a crystal structure schematically. [11]

The condition for interfering thus depends on the interplanar spacing and a specific angle. This diffraction pattern is unique for each crystal and different orientation planes, therefore it is a good way to analyze which crystal orientations are present in the measured samples. [11]

3.6 Scanning electron microscope

The scanning electron microscope (SEM) is an instrument that creates magnified images of inserted samples on microscopic scale with resolutions of below 1 nm. The SEM uses a finely focused beam of electrons which is shot at the surface of a sample, the electrons interact with the atoms at various depths of the sample. These interactions provide two important outgoing electron products among others: back-scattered electrons and secondary electrons. Back-scattered electrons are electrons that are reflected from the sample by elastic scattering. The electrons have a relatively high energy and thus emerge from deeper locations within the sample. Secondary electrons are electrons that escape the atoms in the sample as consequence of the electron beam. These electrons are relatively low in energy and highly localised at the point of impact of the electron beam. Multiple detectors measure the signals sent by both different classes of electrons. The back-scattered electron detector is insensitive to the low energy of the secondary electrons whereas the secondary electron detector measures both signals. The data of both classes of detector is used to generate a surface image. [29]

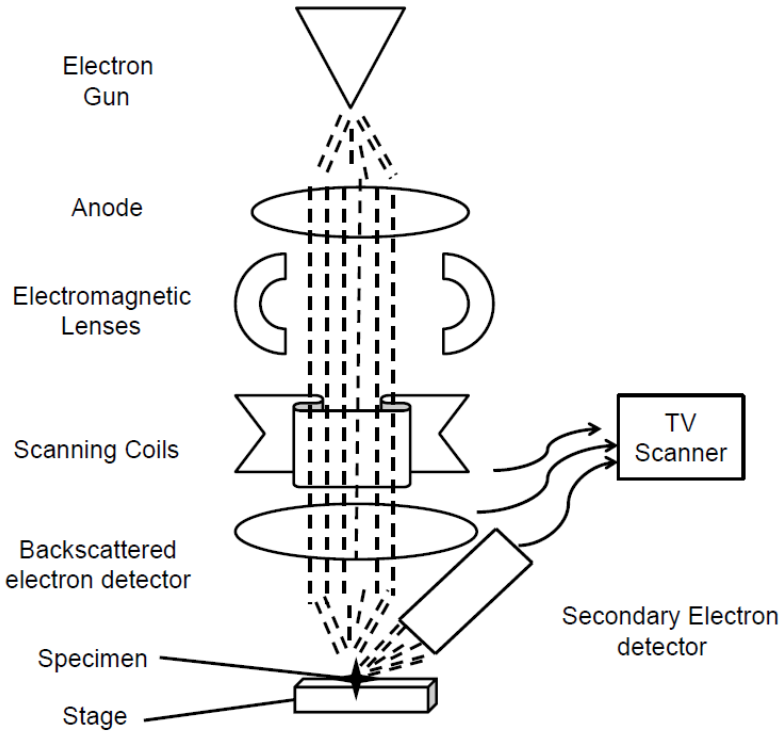

Figure 3.7: Schematic of a SEM setup. [30]

3.7 Seebeck measurement

The Seebeck coefficient is measured using a self-made setup of IMS. In order to measure the Seebeck coefficient, a temperature gradient in the sample is needed and the induced potential should be measured in order to determine the Seebeck coefficient given by equation 2.1.

The setup, as seen in figure 3.8, consists of two Peltier elements that can be cooled and heated by applying a current. At two points on the sample, the temperature and potential are measured using a thermocouple. The thermocouples are connected to a reference bath of liquid nitrogen in order to keep the probes at a constant temperature to accurately measure differences in the sample. The system measures the temperature difference at 6 different Peltier currents. By analyzing the linear regression of the data and compensating for the probes, the Seebeck coefficient can be determined.

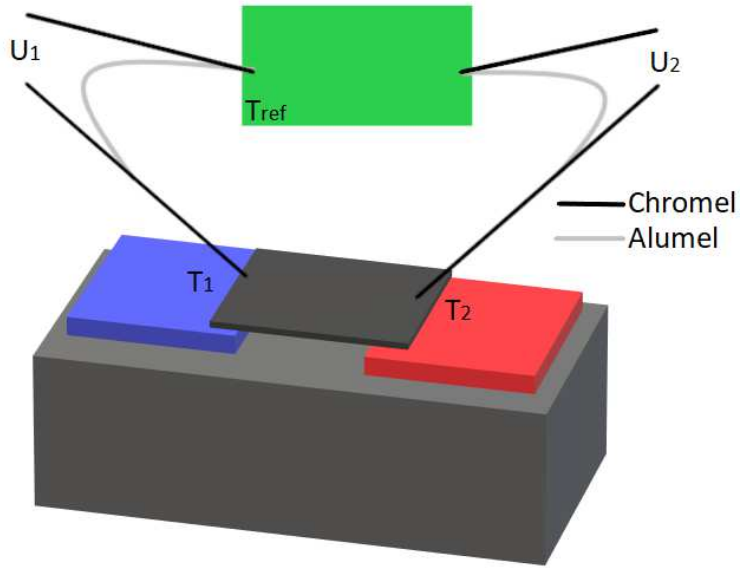

Figure 3.8: Schematic of the Seebeck setup to determine the Seebeck coefficient of a given sample, based on schematic provided.

3.8 Electrical properties

In order to measure the carrier concentration, mobility and resistivity of a sample a combination of the Hall effect and the van der Pauw method is used in the same experimental setup.

3.8.1 Van der Pauw method

The van der Pauw method allows you to measure the (sheet) resistivity. A simple geometry as seen in figure 3.9 can be used to do these measurements. To reduce errors, the sample should be as symmetrical as possible and the sample thickness should be much less than the width or length of the sample. To perform a measurement, a current I is induced between two contact points on a side of the sample. The voltage is measured between the opposite two contact points. This is done for all sides and all directions, giving a total of 8 measurements. The sheet resistance is than given by equation 3.2.

$$R_s = \frac{\pi R}{ln(2)} \tag{3.2}$$

Where R_s is the sheet resistance, and R is the average resistance of all 8 measurements.

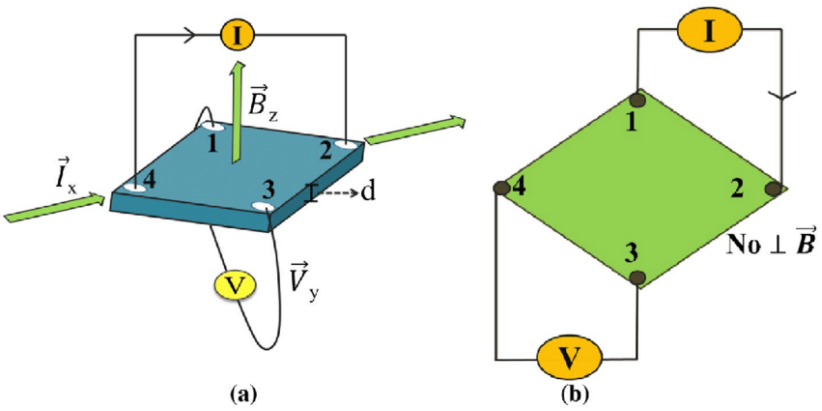

Figure 3.9: Schematic graphic of the Hall effect measurement (a) and van der Pauw method (b). [31]

3.8.2 Hall effect

The Hall effect is a direct result of the Lorentz force as given in equation 3.3.

$$\mathbf{F_L} = q(\mathbf{E} + \mathbf{v} \times \mathbf{B}) \tag{3.3}$$

Where F_L is the Lorentz force, q is the elementary charge, E is the electric field and B is the magnetic field. When applying a magnetic field, a charged particle experiences this Lorentz force proportional to the strength of the field and direction. In the configuration as seen in figure 3.9(a), a current is induced over the diagonal and a magnetic field in the z-direction. Depending on the carrier charge, either positive or negative, the current will deflect accordingly. Since the current is not flowing

straight anymore, a potential difference is created in the sample. This potential is measured over the other diagonal. The magnitude of the Hall voltage (V_H) can be given by equation 3.4.

$$V_H = \frac{IB}{qnd} \tag{3.4}$$

Where n is the charge density and d is the sheet thickness. To measure the Hall voltage, the potential is measured for both diagonals in both directions with positive and negative magnetic field giving the following relations for the voltage differences:

$$V_{13} = V_{13+} - V_{13-} \tag{3.5}$$

$$V_{24} = V_{24+} - V_{24-} \tag{3.6}$$

$$V_{31} = V_{31+} - V_{31-} \tag{3.7}$$

$$V_{42} = V_{42+} - V_{42-} \tag{3.8}$$

$$V_H = \frac{V_{13} + V_{24} + V_{31} + V_{42}}{8} \tag{3.9}$$

Where a positive V_H indicates that the material is a p-type and if negative a n-type. Knowing V_H, the carrier concentration can be calculated using equation 3.4. [11]

Chapter 4

Results & Discussion

All samples were evaluated and analyzed for structural and thermoelectric properties using the techniques as explained in chapter 3. It will be discussed whether the samples have grown as expected in section 2.3 by using AFM images and XRD analysis. Thermoelectric measurements will also be reported and analyzed. The eventual goal in this chapter is to compare the powerfactors of the different samples and report other findings in structural and thermoelectric parameters. Analyzing these results could help in determining which substrate seems the most promising for acquiring a high ZT and thus which material should be researched more thoroughly.
Before the results will be presented and discussed, the samples will be labeled with MW1XX from now on as seen in table 4.1. Apart from the different substrates and the fact they were grown in different batches in the PLD, the growing conditions were exactly the same.

Table 4.1: Sample names with according substrate and batch number in the PLD system

Sample name	Substrate	Batch	Sample name	Substrate	Batch
MW107	STO (001)	1	MW117	MgO (001)	3
MW114	STO (001)	2	MW118	DSO (110)	3
MW115	STO (110)	2	MW119	NSO (110)	3
MW116	STO (111)	2	MW120	ZnO (0001)	3

4.1 Structural analysis

As mentioned in section 3.3, the samples were grown using PLD. In this procedure the same growth conditions have been used, only the substrates differed. After

the samples were grown, they were analyzed structurally using AFM en XRD in order to see if the phases predicted were grown. Also, from MW107 and MW120 cross-sectional SEM images have been made and thus is also used in the structural analysis. From all samples 4 different images were made using AFM. The sizes of the images were 1x1, 3x3, 5x5 and 10x10 μm and were all taken at different locations on the sample to get a variety of images. This was done to get a better picture of the whole surface and not for example only looking at a damaged or dirty part of the surface. All images were edited and processed using Gwyddion software. The roughness of the surface was also extracted using this software. All samples were also analyzed using XRD techniques. MW107 has been measured using a different XRD setup, causing difference in peak shapes and intensities as it uses a monochromator in comparison to the other XRD setup which does not use one. However, the location of the peaks should not be influenced by this difference.

4.1.1 Reproducibility sample grown on STO (001)

First of all, the MW114 and MW107 will be compared to see whether the samples have grown similarly. These two samples are grown on the same substrate with the same target and same conditions using the PLD setup and thus is expected to have a similar structure. This is important as growing a sample should be reproducible, so other researchers also get the same results. Keep in mind, they were grown in different batches, where MW107 was the only sample in one batch and MW114 was one of three samples in the other batch. Also, between the growing of these two batches the PLD system was cleaned which could influence the growth of the samples. Although the samples were grown with these small differences, this should not influence the growth too much and still create reproducible samples.

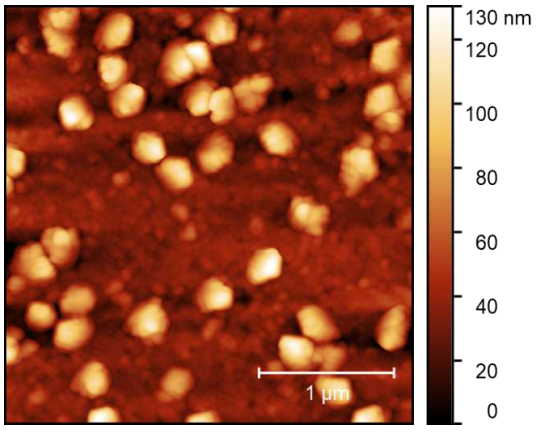

(a) AFM image of MW107 3x3μm.

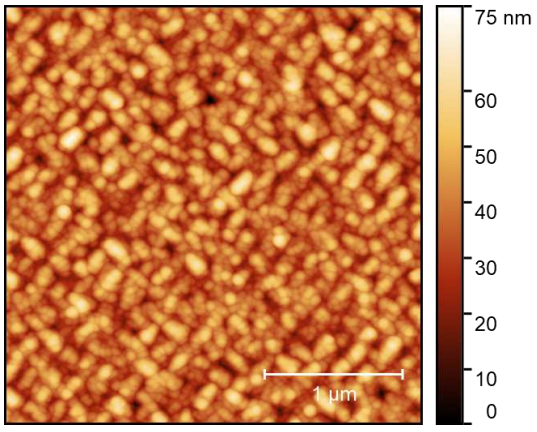

(b) AFM image of MW114 3x3μm

AFM results

As seen in figures 4.1a and 4.1b the structures are clearly not the same on first sight. Looking at the MW114 sample, structures with a 90° angle with respect to each other which could be ZnO $(11\bar{2}0)$. This as there is way more ZnO present on the sample and as seen in figure 2.8b the ZnO orders itself in a 90° angle with respect to itself. The visually less ordered structures in smaller amounts could be the LSMO growing on the substrate. In figure 4.1a these structures of ZnO and LSMO are less obvious present. Quite notable are the big particles on the surface, causing a relatively high roughness of the sample as seen in table 3.1. MW107 has a root mean squared roughness of 17nm where MW114 only has a roughness of 9.3nm. Since the conditions of growing MW107 and MW114 are the same, it is remarkable that this effect is not, or at least a lot less, seen on sample MW114 in the AFM images. Also, the pattern of structures as seen in MW114 is not as clearly seen in MW107 in the AFM images. However, this does not mean it is not there. Due to the bigger particles on the surface, the resolution around those structures is decreased and thus is hard to observe the underlying structure on this image.

Table 4.2: The roughness of the samples extracted from AFM images using Gwyddion software

Sample	RMS roughness (nm)
MW107	17
MW114	9.3
MW115	9.5
MW116	3.7
MW117	23
MW118	30
MW119	34
MW120	13

SEM results

The big particles as seen on the AFM image of MW107 in figure 4.1a are also observed on a SEM image made of the sample in figure 4.2. As the majority of the sample contains ZnO (90%) the light structure is ZnO and the dark structure consequently is LSMO. It is suspected that a different ZnO orientation has grown on top of the surface, which are the cube like structures in a 45° angle on the surface in the SEM image. If this cube like structure indeed is a different orientation, they

should be able to be observed by the XRD. Something else that draws attention on the SEM image, is the LSMO layer grown right on top of the substrate. The VAN structure does not grow on the STO layer but on the LSMO layer. In that top layer, pillars of LSMO with a varying width of approximately 5-50nm can be observed in the ZnO matrix. Unfortunately, as there are no SEM images of MW114 the structures cannot be compared.

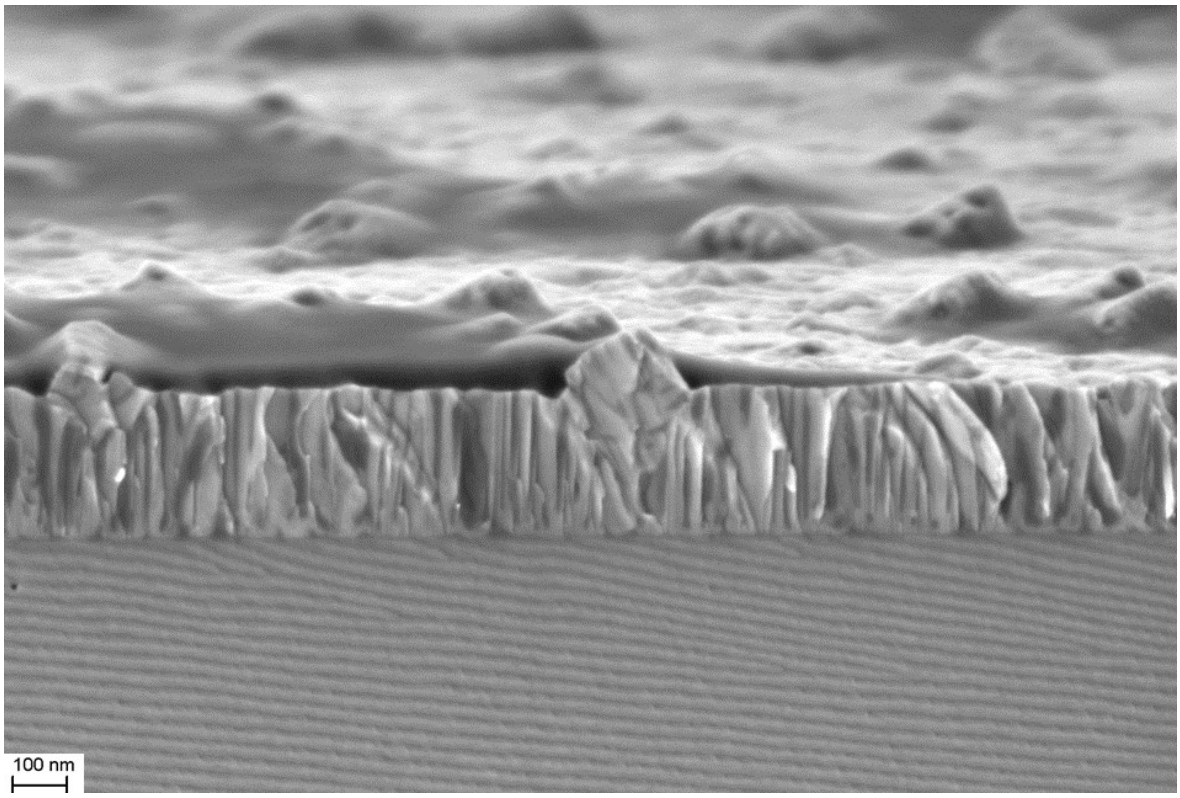

Figure 4.2: Cross-sectional SEM image of sample MW107.

XRD results

Looking at the XRD analysis as seen in figure 4.3, it can clearly be seen that the same phases have been formed in both samples from the peaks which are present in both scans, indicating reproducibility. The presence of ZnO $(11\bar{2}0)$ confirms the predicted growing orientation in section 2.3. The presence of ZnO (0002) in the XRD scan 4.3 confirms that a different orientation of ZnO has grown on the sample and probably are the cube like structures. As both XRD scans were made in different XRD setups, only the peak position can be compared. However, looking at the ratio between the ZnO $(11\bar{2}0)$ and ZnO (0002) peak intensities, more crystalline ZnO (0002) is present in the MW107 sample which is in line with the big particles observed on AFM and SEM images. However, since we lack the SEM data of MW114

this can not be completely proven yet. The difference in these results could be explained by the fact that the laser window of the PLD system was cleaned between the growth of both samples, resulting in different laser intensities between both depositions. The difference between the amount of samples in one batch could also have influenced the growth. This due to the position of the samples with respect to the plasma plume. When more samples are grown in the same deposition, the samples are not aligned precisely in the center of the plasma plume resulting in less material on the sample and a gradient of material.

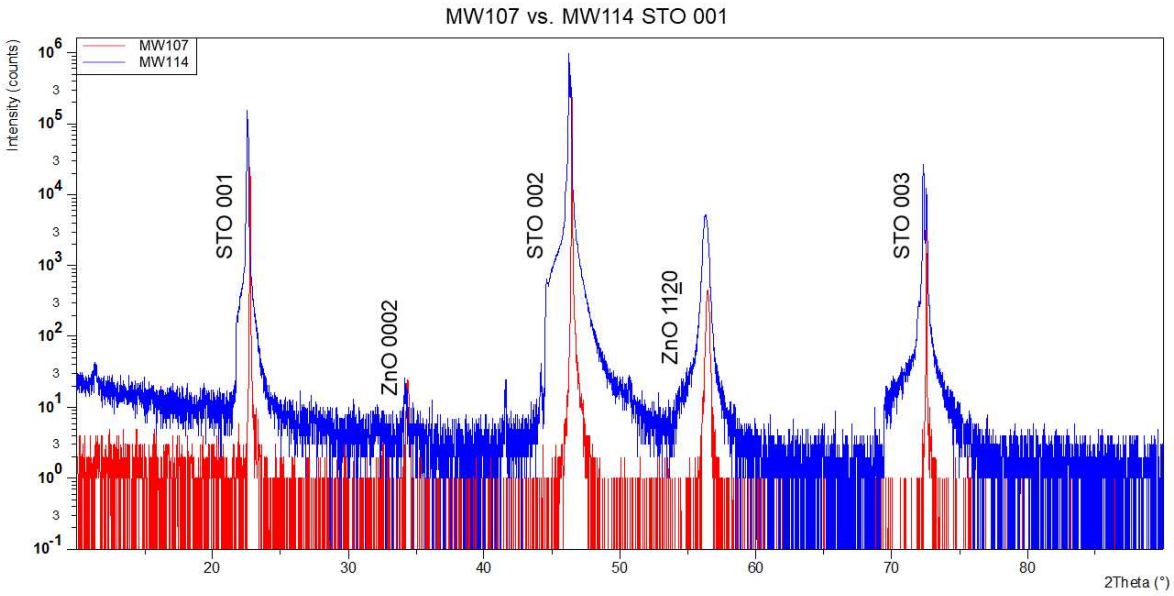

Figure 4.3: XRD comparison of MW107 and MW114 using two different XRD setups.

4.1.2 Influence of STO substrate orientation

Three samples, MW114, MW115 and MW116 were grown on STO with three different orientations, (001), (110) and (111). As discussed in 2.3, there is expected that the LSMO will grow according to the STO orientation as the lattice parameters of LSMO and STO are very similar. So, the LSMO (001) orientation is favored on the STO (001) substrate and so on. A structure as seen in figures 2.8b, 2.8c and 2.8d is also expected with the according ZnO phases.

AFM results

As seen in figures 4.4a, 4.4b and 4.4c the grown structures differ from each other. They resemble the ordering like shown in figures 2.8b, 2.8c and 2.8d indicating that the ZnO orientations have grown as expected on the STO substrates. The roughness of MW116 is low with 3.7nm in comparison to MW114 and MW115 with a roughness of 9.3 and 9.5nm as seen in table 3.1.

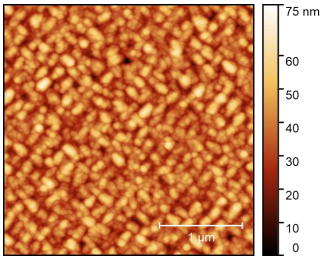

(a) AFM image of MW114 3x3μm.

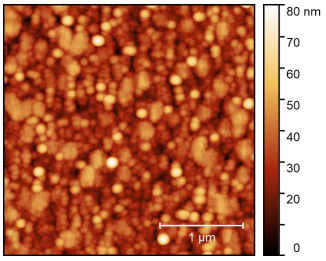

(b) AFM image of MW115 3x3μm

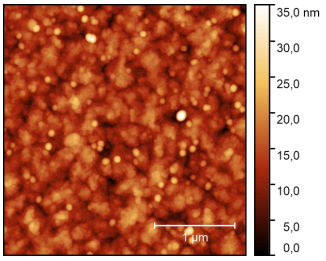

(c) AFM image of MW116 3x3μm

XRD results

From the peak intensities seen in the XRD scans in figure 4.5 the expected orientations have grown on the STO substrate samples. However, in sample MW116 something interesting occurs as seen in its respective scan in figure 4.5. Significantly high intensities are measured for the LSMO (011) orientation which was not expected in the first case. This orientation has a high lattice mismatch with the substrate but it could be possible it can grow well on an other material formed. As seen in figure 2.8c ZnO is expected to grow in the (0001) orientation on STO (110), which is also seen in the XRD scan. As LSMO and STO share very similar lattice parameters, it only makes sense that LSMO (110) could also grow with a relatively low lattice mismatch on ZnO (0001) as also predicted for MW120, which could explain that this particular orientation is present on MW116.

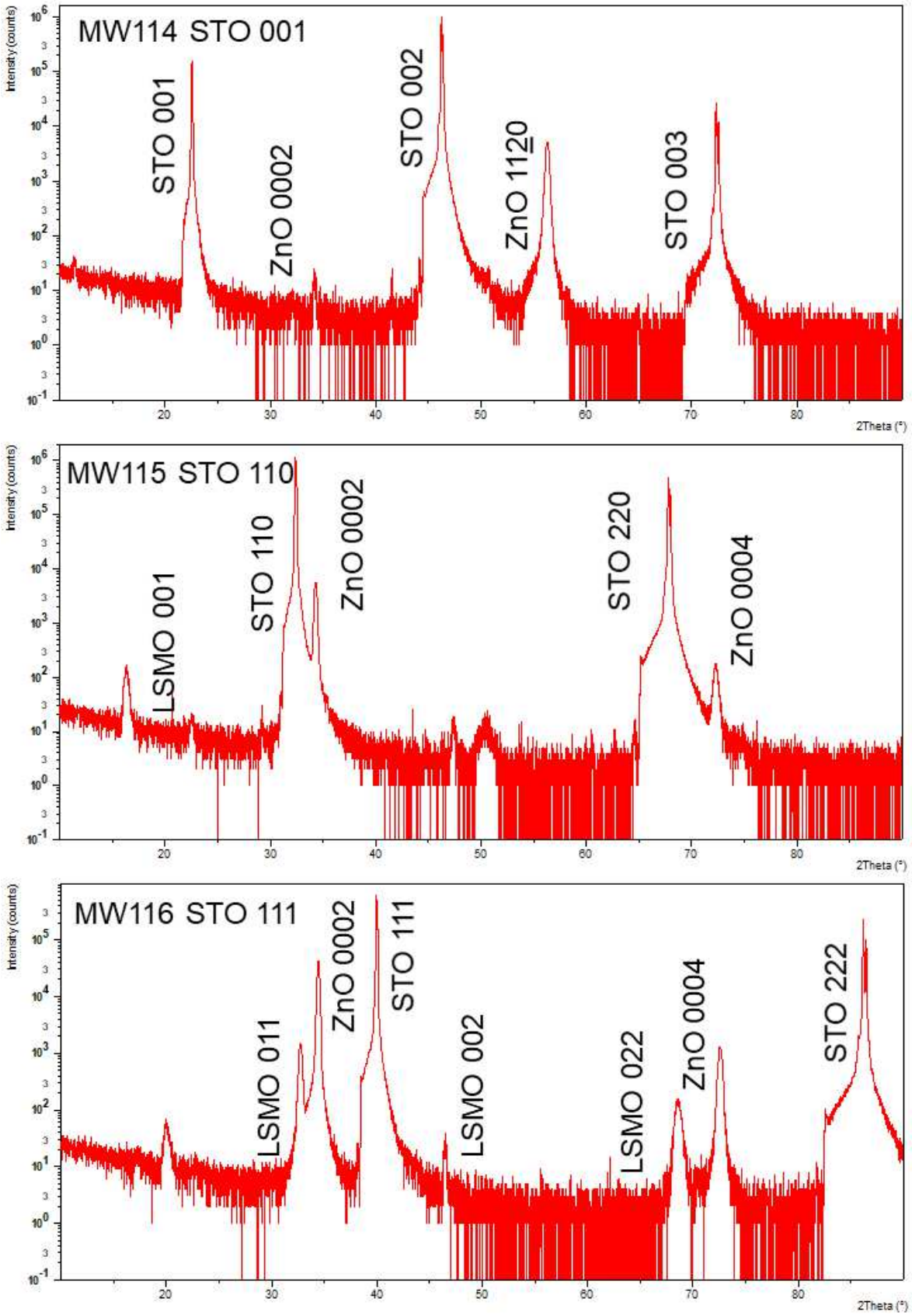

Figure 4.5: XRD scans of MW114, MW115 and MW116.

4.1.3 Scandate substrates

As DSO and NSO are very similar substrates, with similar crystal structure and lattice parameters, these samples will be compared. It is expected that the grown films look similar in the AFM and that the same phases are grown. The AFM images as seen in figures 4.6a and 4.6b are very comparable. Both samples show the same size and shape of structures grown on the sample. It is notable that the amount of these structures is a lot more on MW119 in comparison to MW118. The cause of this is yet unclear. In figure 4.7 the peak intensities show that the expected orientations of LSMO (001) and ZnO (11$\bar{2}$0) have grown on the films. As the in plane spacing for DSO 220 matches LSMO more than NSO, the peak pair of LSMO and DSO is closer in comparison with the NSO sample.

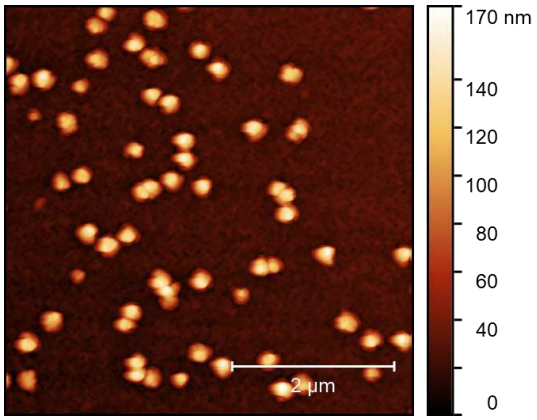

(a) AFM image of MW118 5x5μm.

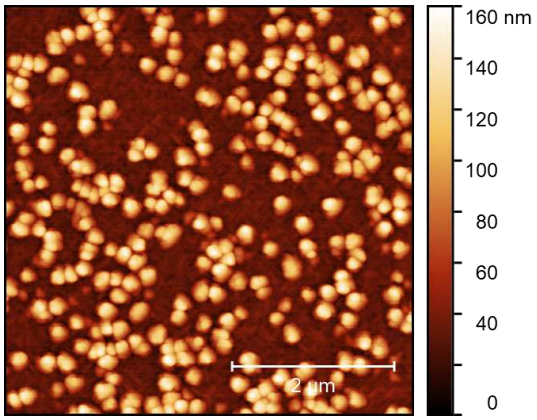

(b) AFM image of MW119 5x5μm

4.1.4 MgO (001) and ZnO (0001)

The last two samples analyzed are the samples grown on MgO (001) and ZnO (0001). As expected for the MgO (001) substrate, LSMO (001) and ZnO (11$\bar{2}$0) are the preferred growing orientations as clearly indicated by the intensity peaks of the XRD scan in figure 4.9. For the substrate ZnO (0001), also the expected orientations have grown. No additional ZnO orientation is formed and LSMO (011) is the preferred orientation as seen in XRD seen in figure 4.9. However, also small amounts of LSMO (001) has grown on the sample. It is yet unclear why this orientation grows, but it grows significantly less than LSMO (001) and thus the expectations still have met.

MgO (001) has the same growing orientation of ZnO as with STO (001) and thus it is expected that a similar structure can be observed in the AFM. So, structures of ZnO (11$\bar{2}$0) with a 90° with respect to itself. This pattern is vaguely seen in figure 4.8a. However, the structure size and shape differ a lot and seems less ordered in

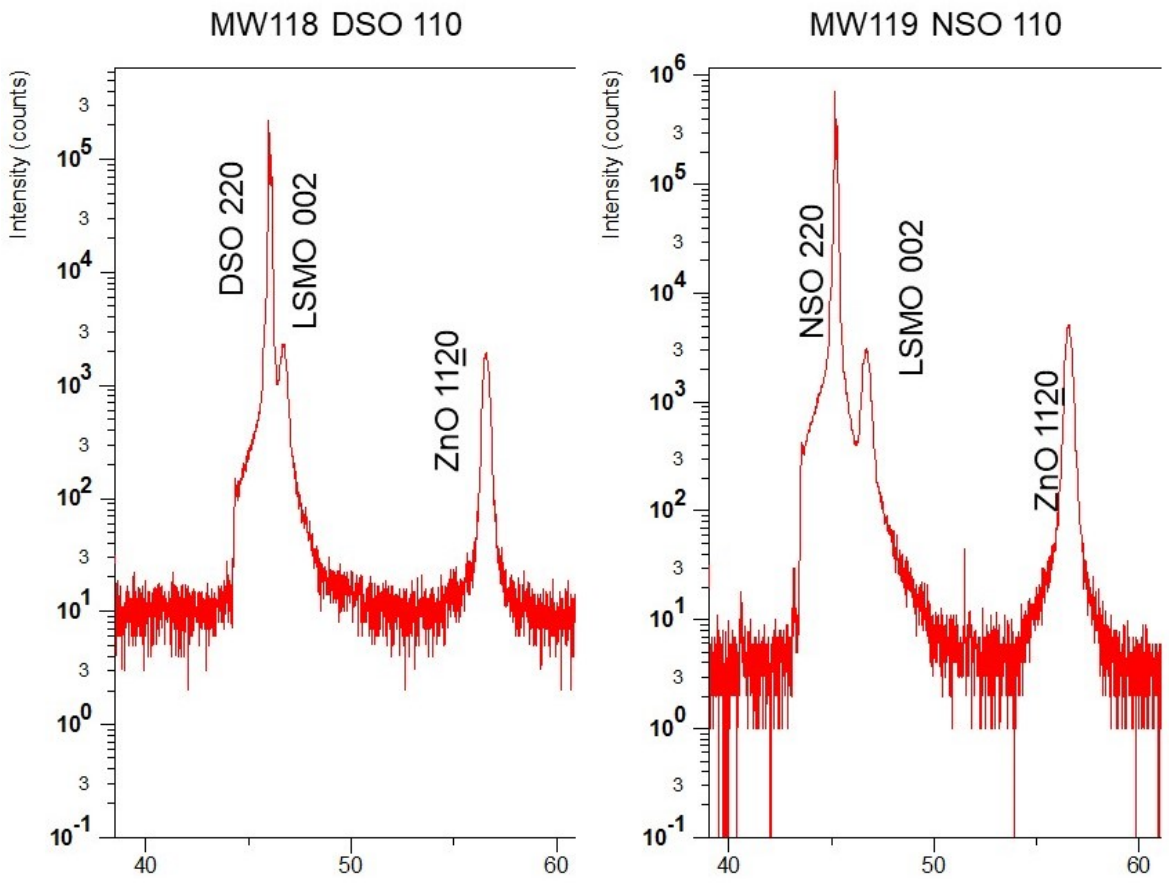

Figure 4.7: XRD scan of MW118 and MW119 comparing peaks around 2θ angle 40-60°

comparison with MW114. For ZnO (0001) it is expected to see hexagonal like structures disrupted by groups of LSMO. Looking at figure 4.8b, clusters of hexagonal like structures are formed and the darker LSMO groups disrupt these clusters.

4.2 Thermoelectric properties

After sputtering Au/Ti contacts, the samples can be measured using the Seebeck setup and the Hall setup. The electrical conductivity, carrier concentration and Seebeck coefficient gives an indication whether the material has the potential to be a good thermoelectric material. This can be indicated by the PF.

4.2.1 Seebeck coefficient

Seebeck measurements are conducted as described in section 3.7. A typical result is seen in graph 4.10. Ideally, for all 6 directions a similar Seebeck coefficient

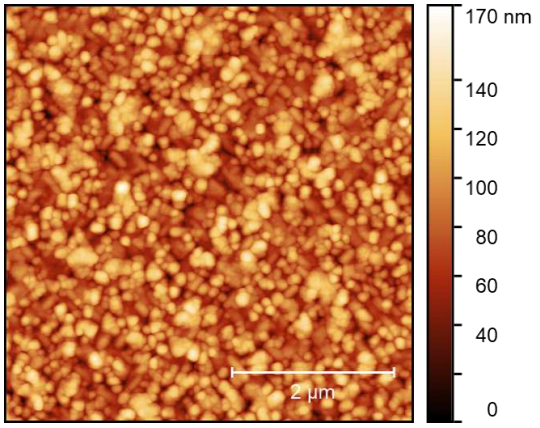

(a) AFM image of MW117 5x5μm.

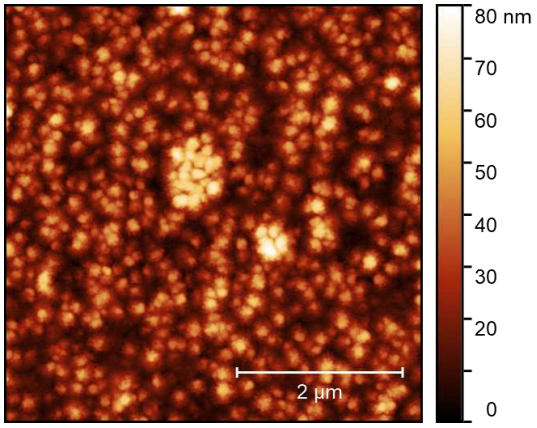

(b) AFM image of MW120 5x5μm

is measured with small errors. However, this was not the case for all samples. For some samples just one direction was a bad measurement with high error. This could mean the probes were not connected properly. But this is not a big problem as long as the other five measurements were okay since the average of the measurements is taken. MW116 is the most notable measurement in this case. Only 1 direction showed a graph with relatively low errors, where the other 5 showed completely different relations and huge errors. Also, structure-wise MW116 is very similar to MW115 and MW114. So, it seems unlikely that the Seebeck coefficient is an order of magnitude larger than the MW115 and MW114 samples as seen in table 4.3. As 5 directions were hard to measure, there seems to be a problem with the sputtered contacts. This also reduces the reliability of the sixth measurement. Therefore, this measured Seebeck coefficient for MW116 should be treated carefully with these errors in mind.
MW120 was measured to have a Seebeck coefficient of $-1020\mu V/K$. This is a Seebeck coefficient of two orders of magnitude bigger than the other samples. Showing great promise for a high PF.

4.2.2 Van der Pauw and Hall

The goal of measuring using the Hall setup is to get an estimation of the carrier concentration and measure the electrical conductivity. However, the in-field measurements were not functioning properly and thus not taken into account. So only the Van der Pauw measurements were conducted and used to calculate the conductivity of each sample. Also, MW120 was measured using a different measurement device.
The electrical conductivities can be found in table 4.3. The errors of MW115 and MW119 are quite high in comparison to the other samples. This could mean bad contacts might have influenced the measurement. The high conductivity of MW120

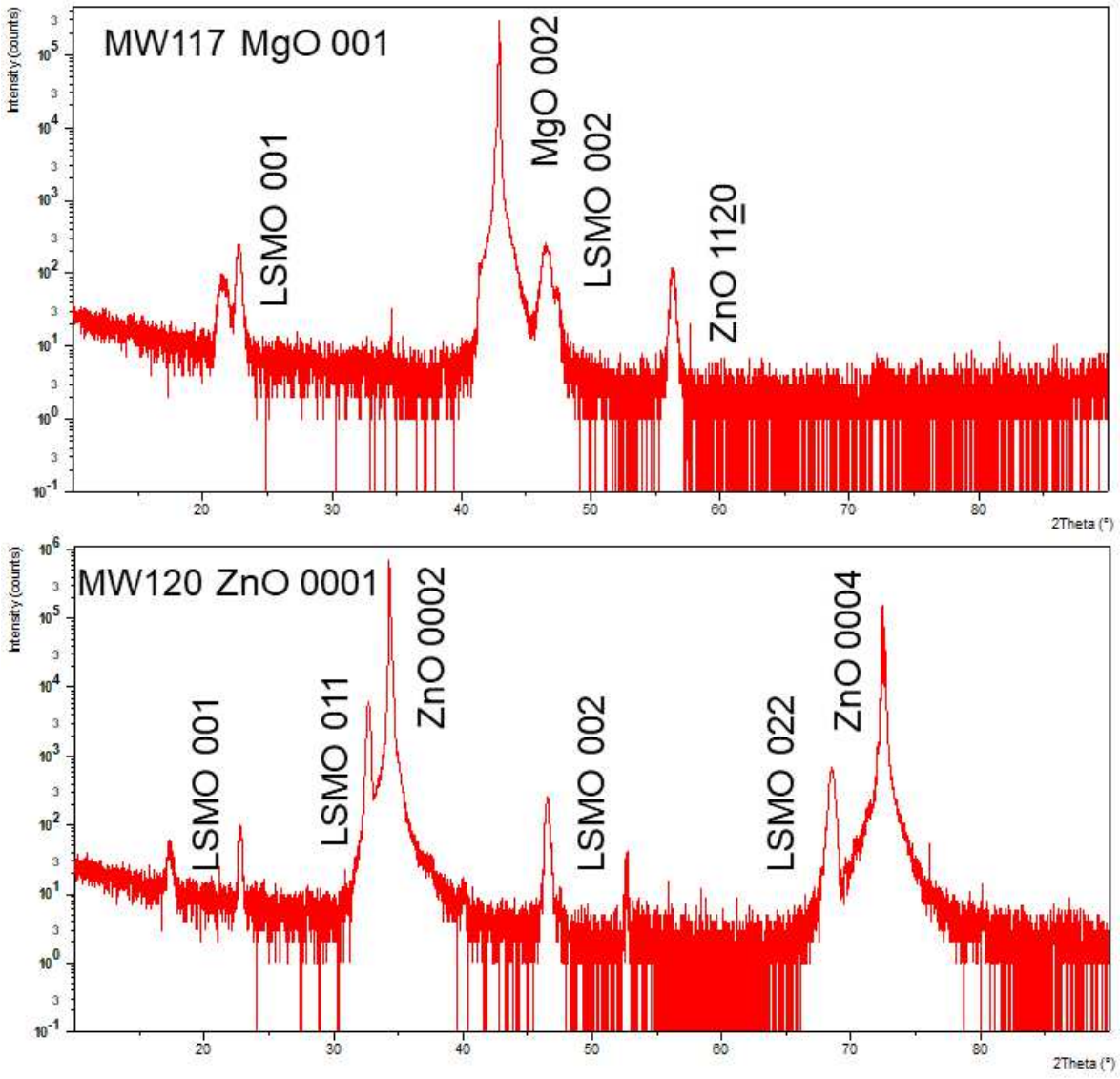

Figure 4.9: XRD scan of MW117 and MW120.

stands out in comparison to the other samples with a conductivity of $23(S/cm)$.

4.3 ZnO (0001) substrate

The sample grown on ZnO 0001 shows significantly higher Seebeck coefficient and electrical conductivity than the other samples. This combination gives a PF of several orders of magnitude higher and comparable to Bi_2Te_3 around room temperature, which is known to be a high performing thermoelectric material. [1] These high measured values in MW120 are the result of a difference in structure in comparison to the other samples. A notable difference can be observed in the two SEM images in figure 4.11. As mentioned earlier, a LSMO layer forms on top of the STO (001)

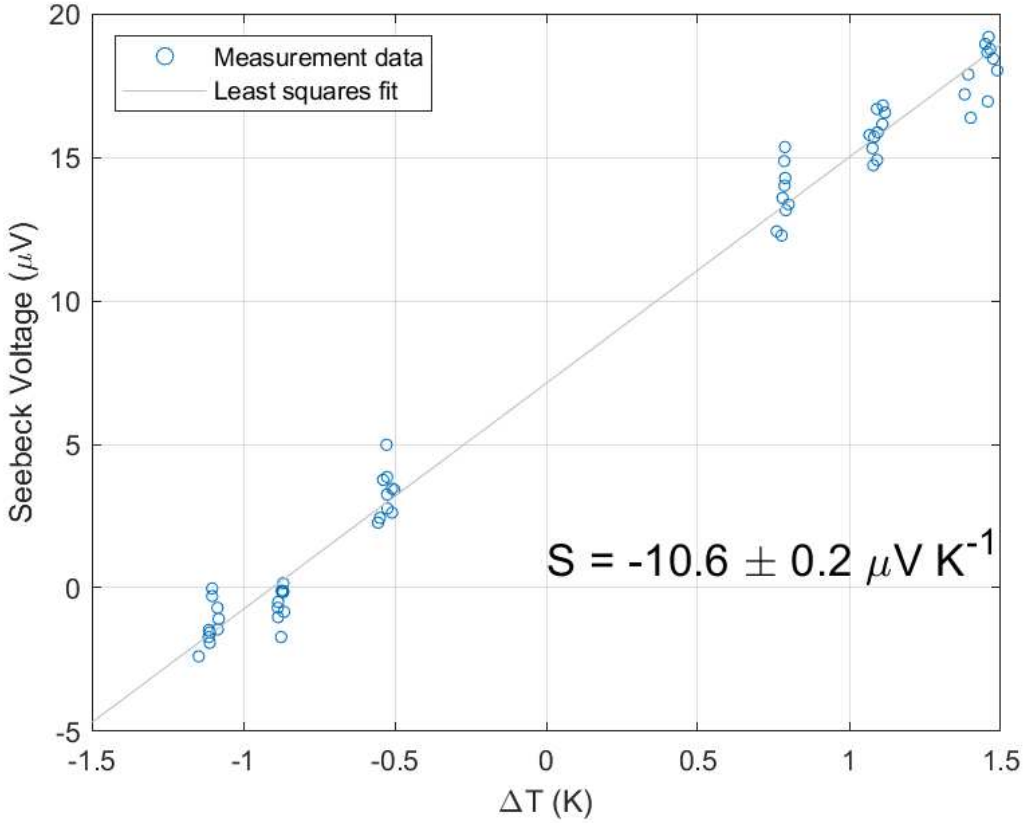

Figure 4.10: Example of graph of a Seebeck measurement processed with MatLab

substrate. However, this effect is not seen on the ZnO 0001 substrate. The VAN structure grows directly on the substrate and clearly LSMO pillars are formed within the ZnO matrix.

As known, all samples from MW107-MW119 contain substrates which match LSMO nearly perfectly and matches ZnO less good. This also holds for MW107 and results in a layer LSMO on the surface of the substrate as seen in figure 4.11, which is the darker layer. LSMO has quite a low Seebeck coefficient, about $-10\mu V/K$, as known from literature. [32] As the Seebeck values from literature correspond to the values measured in samples MW107-MW119 it is suspected the Seebeck coefficient is only measured in the LSMO layer and not the structure on top. The same holds for the electrical conductivity, where literature reports values in the range of $1S/cm$ for LSMO as is also measured. [33] As the measured results are so comparable for all samples MW107-MW119, it gives reason to believe this LSMO layer has grown in all samples. However, due to the lack of the SEM images of the other samples this cannot be completely proven yet.

The film grown on ZnO 0001 does not show this LSMO layer in figure 4.11 which can be explained by the fact that ZnO grows better on ZnO than LSMO. Since this

Table 4.3: Seebeck coefficients, electrical conductivity's and PF's of grown samples

Sample	$S\ (\mu V/K)$	$\sigma\ (S/cm)$	$PF\ (\mu W/(cmK^2)$
MW107	-10.2±0.7	0.77±0.036	8.0E-5±1.1E-5
MW114	-10.4±0.3	2.1±0.002	2.3E-4±1.4E-5
MW115	-10.7±1.9	0.26±0.229	3.0E-5±2.8E-5
MW116	-121±9	0.24±0.072	3.5E-3±1.2E-5
MW117	-10.7±1.3	0.94±0.024	1.1E-4±2.7E-5
MW118	-8.8±1.7	0.33±0.085	2.6E-5±1.2E-5
MW119	-11.6±1.6	0.44±0.271	5.9E-5±4.0E-5
MW120	-1020±53	23±1.5	24±2.9

LSMO layer is not formed, the measured values are very different. The Seebeck coefficient and electrical conductivity measured are more in the range of ZnO as found in literature. [34] This makes sense as 90% of the film grown contains ZnO.

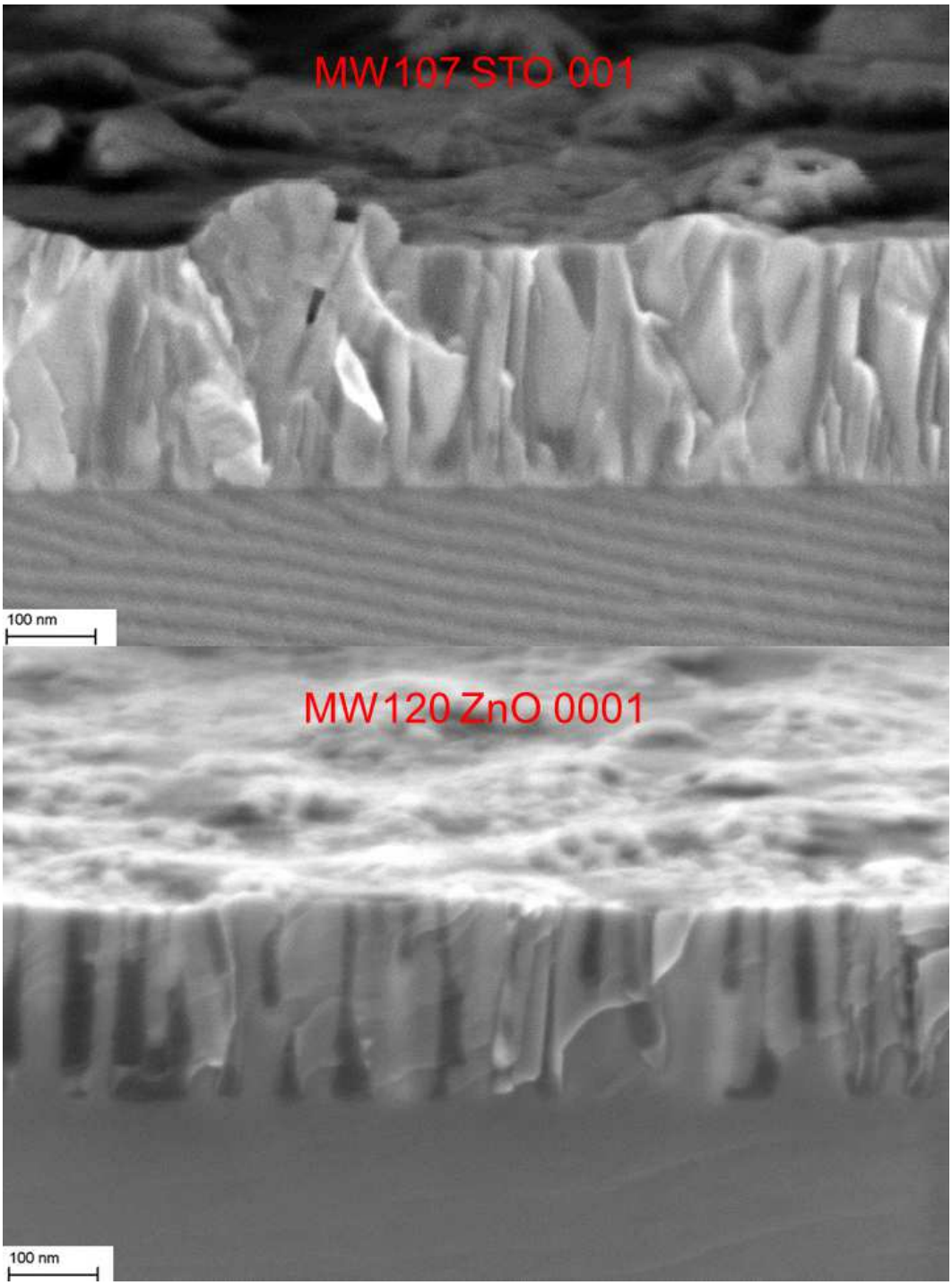

Figure 4.11: SEM images of MW107 and MW120.

Chapter 5

Conclusions and recommendations

5.1 Conclusions

Eight samples were evaluated on their structural and thermoelectric properties where one was functioning as a reference sample. All samples were grown in similar growing conditions on different substrates. In order to perform Seebeck and Van der Pauw measurements, Au/Ti contacts were sputtered on the corners of the samples.

All samples were structurally analyzed using AFM and XRD techniques. The XRD graphs confirmed which phases of the target have grown on the sample as predicted. The surface roughness showed that the samples were flat.

The Seebeck measurements were conducted and generally showed a similar behaviour for 6 measurements with low errors. Sample MW116 showed very inconsistent results giving rise to suspect that the contacts were bad and thus concluding its result is not reliable. In these measurements for MW107-MW119 all showed comparable relatively low Seebeck coefficients of $-10\mu V/K$ which is comparable with S found in literature for LSMO. These low S are probably the result of a LSMO layer grown on the substrate as was seen in the SEM image of MW107. Thus it has not succeeded to grow a VAN structure directly on the substrate. However, the pillar structure of LSMO in the matrix of ZnO was observed above the LSMO layer. As the samples MW107-MW119 showed similar behaviours, it is suspected this same LSMO layer has grown as well with the VAN structure on top. Due to the lack of SEM images of the other samples, this cannot be proven completely yet. The Seebeck coefficient of MW120 was two orders of magnitudes larger with $-1020\mu V/K$. The SEM image shows that is has succeeded to grow a VAN structure directly on the substrate. Due to the absence of the LSMO layer, the Seebeck coefficient changed significantly.

The Hall setup eventually was only used to conduct Van der Pauw measurements as the Hall data was unreliable and the setup was partially defect. MW107-MW119 all showed low electrical conductivities of $0.2 - 2S/cm$ and some with high errors. These values correspond with the electrical conductivity of LSMO as found in literature. Therefor, these results again are the effect of the LSMO layer grown directly on top of the substrate. MW120 showed a high electrical conductivity of $23S/cm$. This significant different value is the result of the absence of the LSMO layer and the successfully grown VAN structure on the sample.

The low results of S and σ in samples MW107-MW119 consequently resulted in low PF's in the range of $1 \times 10^{-3}\mu W/(cmK^2)$. MW120 however showed a promising PF of $24\mu W/(cmK^2)$ which is in the range of the high-performing thermoelectric material Bi_2Te_3 at room temperature. [1]

5.2 Recommendations

MW120 using a ZnO (0001) substrate with LSMO ZnO (1:9) shows very promising thermoelectric properties and thus is a material of great interest. Therefore, this material should be researched more thoroughly. There should be researched how certain growing parameters, like the temperature of the substrate and laser frequency, influence the growth of this structure and determine how these parameters influence the thermoelectric parameters in order to optimize them.

Also, a sample with Al doped ZnO should be grown and researched to see how the electrical conductivity is influenced. Literature suggests that the electrical conductivity could increase with an order of magnitude, having a great influence on the PF. [35]

The last step in order to determine the ZT value is to measure its thermal conductivity. These measurements cannot be done at the University of Twente but as it is a very interesting material with high PF's this last property should be measured somewhere else in order to determine the ZT. This last parameter which show if this material has the potential of being a good thermoelectric material.

In order to prove that all other samples (MW114-MW119) did also grow the expected LSMO layer, these should be checked using the SEM. If there can be confirmed these LSMO layers are grown, the effects can be related with each other and

gives more insight of how to grow VAN structures.

In some measurements the bottleneck were the contacts of the samples. There should be researched how to improve these contacts in order to measure consistently.

Bibliography

[1] J. Cha, C. Zhou, S.-P. Cho, S. H. Park, and I. Chung, "Ultrahigh power factor and electron mobility in n-type bi2te3–x%cu stabilized under excess te condition," *ACS Applied Materials & Interfaces*, vol. 11, pp. 30999–31008, Aug 2019.

[2] "The internet of things: Mapping the value beyond the hype.." Mckinsey, https://www.mckinsey.com/~/media/McKinsey/Industries/Technology%20Media%20and%20Telecommunications/High%20Tech/Our%20Insights/The%20Internet%20of%20Things%20The%20value%20of%20digitizing%20the%20physical%20world/The-Internet-of-things-Mapping-the-value-beyond-the-hype.pdf, accessed at 21-10-2020.

[3] M. F. Maulana, S. Adhy, N. Bahtiar, and I. Waspada, "Development of a smart parking system based on internet of things using object-oriented analysis and design method," *Journal of Physics: Conference Series*, vol. 1524, p. 012111, apr 2020.

[4] A. Khanna and R. Anand, "Iot based smart parking system," in *2016 International Conference on Internet of Things and Applications (IOTA)*, pp. 266–270, 2016.

[5] Hongwei Wang and Wenbo He, "A reservation-based smart parking system," in *2011 IEEE Conference on Computer Communications Workshops (INFOCOM WKSHPS)*, pp. 690–695, 2011.

[6] K. Biswas, J. He, I. D. Blum, C.-I. Wu, T. P. Hogan, D. N. Seidman, V. P. Dravid, and M. G. Kanatzidis, "High-performance bulk thermoelectrics with all-scale hierarchical architectures," *Nature*, vol. 489, pp. 414–418, Sep 2012.

[7] A. Chen, W. Zhang, F. Khatkhatay, Q. Su, C.-F. Tsai, L. Chen, Q. X. Jia, J. L. MacManus-Driscoll, and H. Wang, "Magnetotransport properties of quasi-one-dimensionally channeled vertically aligned heteroepitaxial nanomazes," *Applied Physics Letters*, vol. 102, no. 9, p. 093114, 2013.

[8] T. Tsubota, M. Ohtaki, K. Eguchi, and H. Arai, "Thermoelectric properties of al-doped zno as a promising oxide material for high-temperature thermoelectric conversion," *J. Mater. Chem.*, vol. 7, pp. 85–90, 1997.

[9] D. M. Cunha, C. M. Vos, T. A. Hendriks, D. P. Singh, and M. Huijben, "Morphology evolution during lithium-based vertically aligned nanocomposite growth," *ACS Applied Materials & Interfaces*, vol. 11, no. 47, pp. 44444–44450, 2019. PMID: 31684722.

[10] A. F. May and B. C. Sales, "Twisting the thermoelectric potential," *Nature Materials*, Jan 2021.

[11] . Callister, William D. Jr. and D. G. Rethwisch, *Fundamentals of materials science and engineering : an integrated approach*. Singapore: Wiley, 5th edition, international student version. ed., 2016.

[12] R. J. D. Tilley, "Understanding solids : the science of materials.," 2013.

[13] G. Snyder and E. Toberer, "Complex thermoelectric materials," *Nature materials*, vol. 7, pp. 105–14, 03 2008.

[14] J. Feng, "Microstructural evolution in spinodal half-heusler thermoelectrics," 12 2014.

[15] R. Anufriev, R. Yanagisawa, and M. Nomura, "Aluminium nanopillars reduce thermal conductivity of silicon nanobeams," *Nanoscale*, vol. 9, p. 15083, 09 2017.

[16] K. Galloway and N. Sammes, "Fuel cells – solid oxide fuel cells — anodes," in *Encyclopedia of Electrochemical Power Sources* (J. Garche, ed.), pp. 17–24, Amsterdam: Elsevier, 2009.

[17] Z. Yi, N. H. Ladi, X. Shai, H. Li, Y. Shen, and M. Wang, "Will organic–inorganic hybrid halide lead perovskites be eliminated from optoelectronic applications?," *Nanoscale Adv.*, vol. 1, pp. 1276–1289, 2019.

[18] K. A. Adegoke, M. Iqbal, H. Louis, S. Jan, M. Anam, and O. Bello, "Photocatalytic conversion of co2using znosemiconductor by hydrothermal method," *Pakistan Journal of Analytical & Environmental Chemistry*, vol. 19, pp. 1–27, 06 2018.

[19] C. Jia, Y. Chen, X. Liu, S. Yang, W. Zhang, and Z. Wang, "Control of epitaxial relationships of zno/srtio3 heterointerfaces by etching the substrate surface," *Nanoscale Research Letters*, vol. 8, p. 23, Jan 2013.

[20] A. Biswas, P. B. Rossen, C.-H. Yang, W. Siemons, M.-H. Jung, I. K. Yang, R. Ramesh, and Y. H. Jeong, "Universal ti-rich termination of atomically flat srtio3 (001), (110), and (111) surfaces," *Applied Physics Letters*, vol. 98, no. 5, p. 051904, 2011.

[21] N. A. Geisse, "Afm and combined optical techniques," *Materials Today*, vol. 12, no. 7, pp. 40–45, 2009.

[22] N. Ishida and V. Craig, "Direct measurement of interaction forces between surfaces in liquids using atomic force microscopy," *KONA Powder and Particle Journal*, vol. 36, 01 2019.

[23] H.-J. Butt, B. Cappella, and M. Kappl, "Force measurements with the atomic force microscope: Technique, interpretation and applications," *Surface Science Reports*, vol. 59, no. 1, pp. 1–152, 2005.

[24] A. Biswas, C.-H. Yang, R. Ramesh, and Y. H. Jeong, "Atomically flat single terminated oxide substrate surfaces," *Progress in Surface Science*, vol. 92, no. 2, pp. 117–141, 2017.

[25] E. Morintale, C.-D. Constantinescu, and M. Dinescu, "Thin films development by pulsed laser-assisted deposition," *Annals of the University of Craiova, Physics*, vol. 20, 01 2010.

[26] S. Vanalakar, A. Galal, V. N. Singh, and H. Min, "A review of nanostructured thin films for gas sensing and corrosion protection," *Mediterranean Journal of Chemistry*, vol. 7, pp. 433–451, 11 2018.

[27] F. Shi, *Introductory Chapter: Basic Theory of Magnetron Sputtering.* 11 2018.

[28] D. Depla, S. Mahieu, and J. Greene, "Chapter 5 - sputter deposition processes," in *Handbook of Deposition Technologies for Films and Coatings (Third Edition)* (P. M. Martin, ed.), pp. 253–296, Boston: William Andrew Publishing, third edition ed., 2010.

[29] J. . Goldstein, D. E. Newbury, J. R. Michael, N. W. M. Ritchie, J. H. J. Scott, and D. C. . Joy, "Scanning electron microscopy and x-ray microanalysis," 2018.

[30] M. Tare, O. Puli, S. Oros, and A. Singh, "Drosophila adult eye model to teach scanning electron microscopy in an undergraduate cell biology laboratory," *Population Data Information Service*, vol. 92, pp. 174–180, 01 2009.

[31] K. Muthusamy, S. Hussain, R. Gopalakrishnan, and k. Vishista, “Influence of solvents on solvothermal synthesis of cu 2 sns 3 nanoparticles with enhanced optical, photoconductive and electrical properties,” *Materials Technology*, vol. 33, pp. 1–7, 09 2017.

[32] C.-S. Park, M.-H. Hong, S. Shin, H. H. Cho, and H.-H. Park, “Synthesis of mesoporous la0.7sr0.3mno3 thin films for thermoelectric materials,” *Journal of Alloys and Compounds*, vol. 632, pp. 246–250, 2015.

[33] R. Kinner, A.-M. Azad, G. Srinivasan, S. Gollapudi, and M. Jain, “Zno/lsmo nanocomposites for energy harvesting,” *Smart Nanosystems in Engineering and Medicine Vol.2 pp3-17 (2012)*, 01 2012.

[34] S. Jantrasee, P. Moontragoon, and S. Pinitsoontorn, “Thermoelectric properties of al-doped zno: Experiment and simulation,” *Journal of Semiconductors*, vol. 37, 09 2016.

[35] Y. Zhang, Y. Yang, J. Zhao, R. Tan, W. Wang, P. Cui, and W. Song, “Optical and electrical properties of aluminum-doped zinc oxide nanoparticles,” *Journal of Materials Science*, vol. 46, pp. 774–780, 02 2011.

Appendix A

AFM

AFM images of the treated substrates NSO, DSO, MgO and ZnO can be found in figure A.1. Looking at the surfaces they are well treated and clear terraces have formed. These substrates are sufficiently flat to grow thin films on.

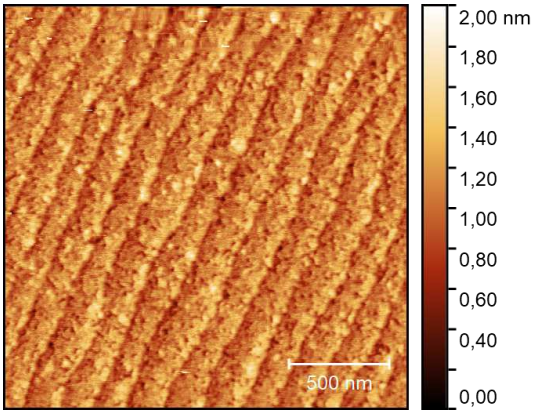

(a) AFM image of treated NSO 2x2μm.

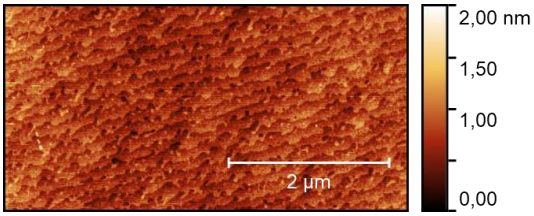

(b) AFM image of treated DSO 3x5μm.

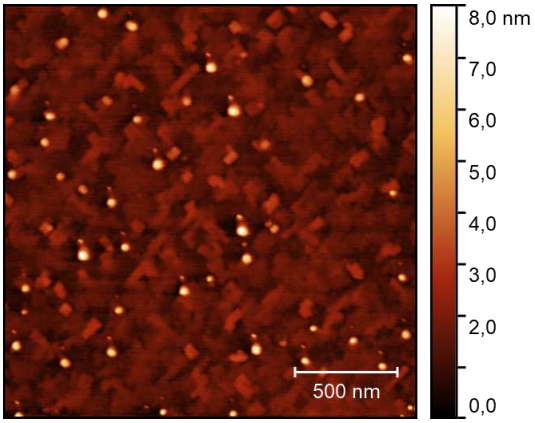

(c) AFM image of treated MgO 2x2 μm

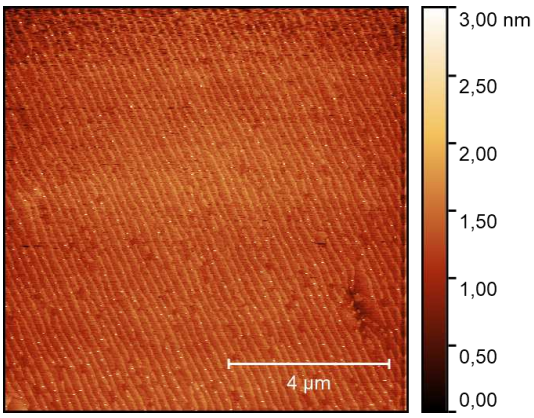

(d) AFM image of treated ZnO 10x10μm

Figure A.1: AFM images of the substrates DSO, NSO, MgO and ZnO after treatment.

Appendix B

Error measurements

During the Seebeck en Van der Pauw measurements, different error calculations have been used. These errors will now be discussed shortly.

B.1 Seebeck error

As explained in section 3.7 the data set of the Seebeck measurement was analyzed using linear regression. A linear fit of the data set was made and the slope calculated. A typical data set can be found in figure B.1. A 95% confidence interval is taken from this data set to calculate the error on the slope.

B.2 Van der Pauw error

Using the Van der Pauw setup, multiple measurements were made. Of these measurements the mean and the standard deviation of this mean given by equation B.1 and B.2 respectively is used to calculate the error. N is the amount of measurements and x_i are the variables in the data set.

$$\bar{x} = \frac{1}{N}\sum_{i=1}^{N} x_i \tag{B.1}$$

$$\sigma_s = \sqrt{\frac{1}{N-1}\sum_{i=1}^{N} (x_i - x)^2} \tag{B.2}$$

To compute the error using earlier measurements, error propagation is needed. When adding two variables, the two errors are additive. But when taking the power or multiplying, this is not the case. When calculating the PF following general relation

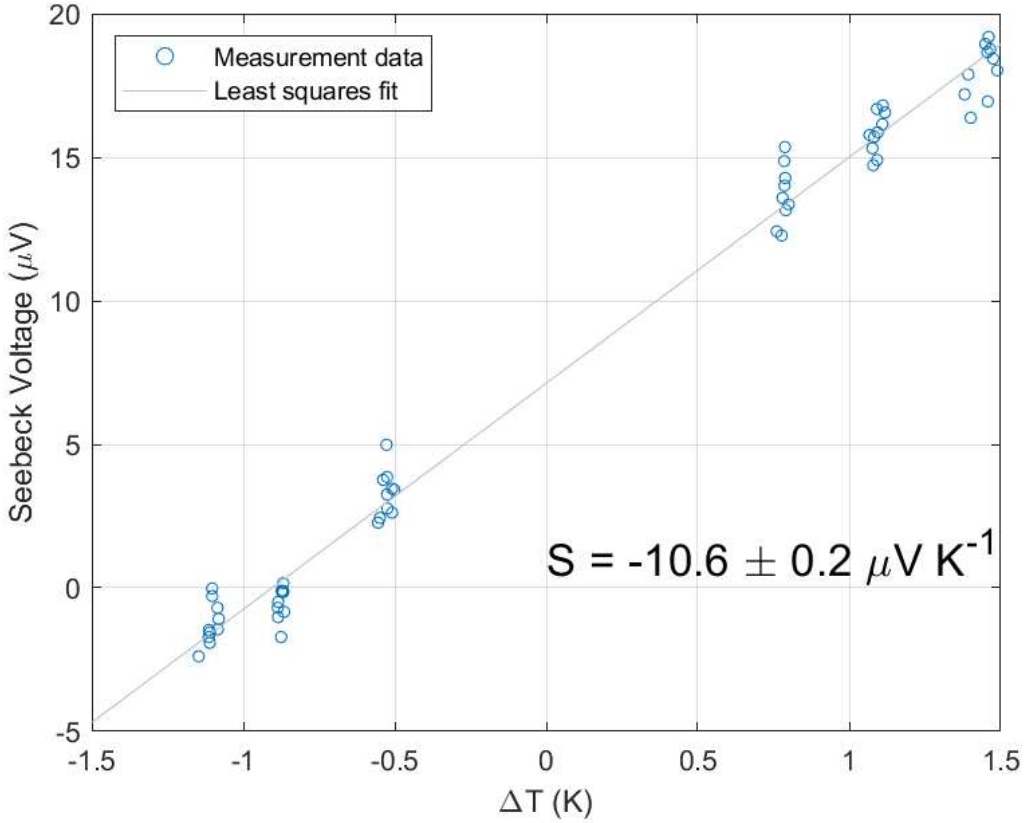

Figure B.1: Example of graph of a Seebeck measurement processed with MatLab.

should be applied. Equation B.3 is a general formula for a certain relation where δz in equation B.4 is its accoring error.

$$z = cx^a y^b \tag{B.3}$$

$$\delta z/z = c\sqrt{(a\frac{\delta x}{x})^2 + (b\frac{\delta y}{y})^2} \tag{B.4}$$

As $PF = \sigma S^2$ equation B.4 becomes equation B.5 to calculate the total error of PF. For all similar cases, these computations have been conducted.

$$error_{PF} = PF * \sqrt{(1\frac{error_\sigma}{\sigma})^2 + (2 * \frac{error_S}{S})^2} \tag{B.5}$$